Analysis of an intense O_3 pollution episode in the Atlantic Coast of the Iberian Peninsula using photochemical modeling: characterization of transport pathways and accumulation processes.

Eduardo Torre-Pascual[1], Gotzon Gangoiti[1], Ana Rodríguez-García[1], Estibaliz Sáez de Cámara[1], Joana Ferreira[2], Carla Gama[2], María Carmen Gómez[1], Iñaki Zuazo[1], Jose Antonio García[1], Maite de Blas[1].

[1]Faculty of Engineering Bilbao, University of the Basque Country (UPV/EHU), Bilbao, 48013, Spain

[2]CESAM & Department of Environment and Planning, University of Aveiro, Aveiro, 3810-193, Portugal

Correspondence to: Eduardo Torre-Pascual (eduardo.delatorre@ehu.eus)

Abstract. A tropospheric O_3 pollution episode over the Atlantic Coast of the Iberian Peninsula during August 2-6 in 2018 has been analyzed. The episode was characterized by a permanent wind shear throughout the entire period, making the observed ozone surface distribution especially difficult to explain. A new methodology is described analyzing upper-level atmospheric parameters, such as temperature, wind direction, wind speed, and O_3 concentrations, added to the traditional use of surface parameters, using WRF-CAMx models and available surface and upper-air observations. Results indicate that the episode was characterized by a first phase of a sudden increase in O_3 concentrations produced by fumigation and interregional transport processes within the Iberian Peninsula, followed by a continental O_3 transport from Europe to the Atlantic Coast. An Atlantic front produced the dissipation of the episode, generating an "ozone front" accompanying the cold front passage across the region.

1. Introduction

Southern European countries are heavily exposed to high tropospheric ozone (O_3) concentrations, particularly those surrounding the Mediterranean Basin (ETC/ACM, 2018; EEA, 2019). Accumulation, transport, and recirculation processes behind these high concentrations have been extensively analyzed in the Western Mediterranean Basin and Eastern Iberia during the last 40 years (Millán et al., 1997; Gangoiti et al., 2001; Querol et al., 2016). The 2020 European air quality report indicated a decrease in O_3 levels compared to previous years. However, levels remained notably high, with maximum concentrations observed in central Europe, certain Mediterranean countries, and Portugal - located on the Atlantic Coast of the Iberian Peninsula (IP) (EEA, 2022). These high O_3 concentrations are due to a combination between the northern mid-latitudes background concentrations (Cuevas et al., 2013; Rodrigues et al., 2021) and the local and regional production favored by the region's circulation weather patterns (Russo et al., 2016) and meteorological conditions, including temperature (Sá et al., 2015) and solar radiation (Silva and Pires, 2022). However, despite their importance, O_3 episodes in the Atlantic Coast, specifically in Northern Atlantic Iberia (NAI) and Western Atlantic Iberia (WAI), have not been examined in detail. In this region, significant episodes of tropospheric O_3 have occurred, with values exceeding the target value defined for the protection of human health defined by the Directive 2008/50/EC (Silva and Pires, 2022). Moreover, considering the more stringent values of the World Health Organization (WHO) air quality guidelines (which are planned to be incorporated into the revised air quality directive by 2035), the situation becomes even more concerning.

In NAI, data from the summer flight campaigns of the European MECAPIP project (Millán et al., 1992, 1997) revealed long-range transport of photochemical pollutants from the English Channel into the Basque Country (BC) (Alonso et al., 2000). Pollutants are usually transported under the typical summer synoptic scenario, with the Azores High extending a ridge of high pressures over the Bay of Biscay and pushing northerly winds over NAI.

Gangoiti et al. (2002, 2006a) showed the importance of vertical layering and transport in the generation of intense O_3 episodes in the BC under a different synoptic situation, with persistent northeasterly winds associated with blocking anticyclones over the British Isles. That work also documented the importation of pollutants into the BC from several European source regions during the build-up of episodes, including the Iberian Peninsula. Valdenebro et al. (2011) showed how O_3 transport efficiency increased after the formation of accumulation layers of polluted air masses aloft, which can travel large distances within a stably stratified Maritime Boundary Layer (MBL) or over the stable nocturnal surface boundary layer over land. The latter study demonstrated that transport from and to the Ebro and Douro valleys, both located in the IP, plays a main role in O_3 episodes in the BC. Sáez de Cámara et al. (2018) documented that O_3 observations in background areas of the BC may have production and transport of local origin from surrounding areas during midday, and a contribution from the arrival of polluted air masses in the afternoon during the accumulation and peak phases.

Past studies for WAI in Portugal showed typical temporal patterns with maximum mean monthly concentrations during spring, and maximum hourly concentrations during summer (Pires et al., 2012). Concentrations are higher in inland and rural areas than in urban regions. However, O_3 episodes, with concentrations above the thresholds defined for the protection of human health, also occur in urban regions. Several studies (Evtyugina et al., 2007; Monteiro et al., 2012, 2016) showed the importance of sea breeze circulation in the build-up of O_3 episodes through the Portuguese coast, pointing to the importance of precursors emitted in coastal areas and O_3 production along the transport towards inland areas. Hertig et al. (2020) showed that in Portugal the occurrence of O_3 and heat wave events had the strongest relationship for eastern and northeastern inflow, highlighting the importance of the advection of O_3 pollution from the continental parts of the Iberian Peninsula. In addition to the regular anthropogenic (e.g., traffic, industry, energy production) and biogenic (natural) sources, extraordinary events such as forest fires play an important role in the O_3 episodes registered in Portugal (Adame et al., 2012).

In this article, for the first time and as far as the authors know, the tropospheric O_3 problem is approached in an integral way for the Atlantic Coast of the Iberian Peninsula. We have selected an O_3 pollution episode lasting five days occurring from August 2nd to 6th, 2018 (see Section 3.3), which affected Spain and Portugal. This episode was characterized by a notable and simultaneous increase in O_3 concentration levels across both the NAI and WAI regions during August 2, high O_3 concentrations during consecutive days until August 6, and final dissipation on August 7. We utilized the modeling system described in Section 2 to examine the local-to-interregional transport and accumulation of O_3 within and between two countries, as well as between these countries and the rest of Europe. Valdenebro et al. (2011) proposed the existence of a potential transport pathway for O_3 and pollutants along the Atlantic axis of the Iberian Peninsula, in NAI. This hypothesis, together with the fact that Spain and Portugal share three main air basins draining from central Iberia into the Atlantic, implies that the analysis should be carried out as a whole for the two regions: Northern Atlantic Iberia (NAI) and Western Atlantic Iberia (WAI), as shown in Figure 1. We expose how interregional transport of O_3 is a key element in explaining the observed evolution of this episode.

1.1 Area Description

The Iberian Peninsula, with Spain and Portugal, has a complex topography with numerous mountain ranges, with an average altitude among the highest in Europe. IP is surrounded by the Bay of Biscay to the North, the Mediterranean Sea to the East, the Mediterranean and Atlantic Ocean to the South, where both meet through the Strait of Gibraltar, and by the Atlantic Ocean to the West (Figure 1). It is separated from the European continent by the Pyrenees Mountain range and a high central plateau largely occupies its surface. The rivers flowing into the sea produce numerous air basins and valleys that are decisive for studying atmospheric pollution due to their particular wind regimes.

To the North, parallel to the coast it is located the Cantabrian Range, with elevations of more than 2,500 m ASL in its central zone. This mountain range extends from West to East to the western end of the Pyrenees and separates the Northern coast of the IP from the Northern peninsular Plateau. Basque Country is in the link between the Northern coast of IP and the Pyrenees, with lower altitude mountains, usually below 1,500 m ASL. To the West of IP, in Portugal, there are two different areas: north of the Tagus River where mountainous areas also predominate, and south with flatter landscapes and a few low mountains. Most of Portugal is below 400 m ASL, and the highest altitudes are in the Serra da Estrela, which forms a continuation of the Spanish Central System. Both countries share the valleys of the Douro, Tagus, and Guadiana rivers.

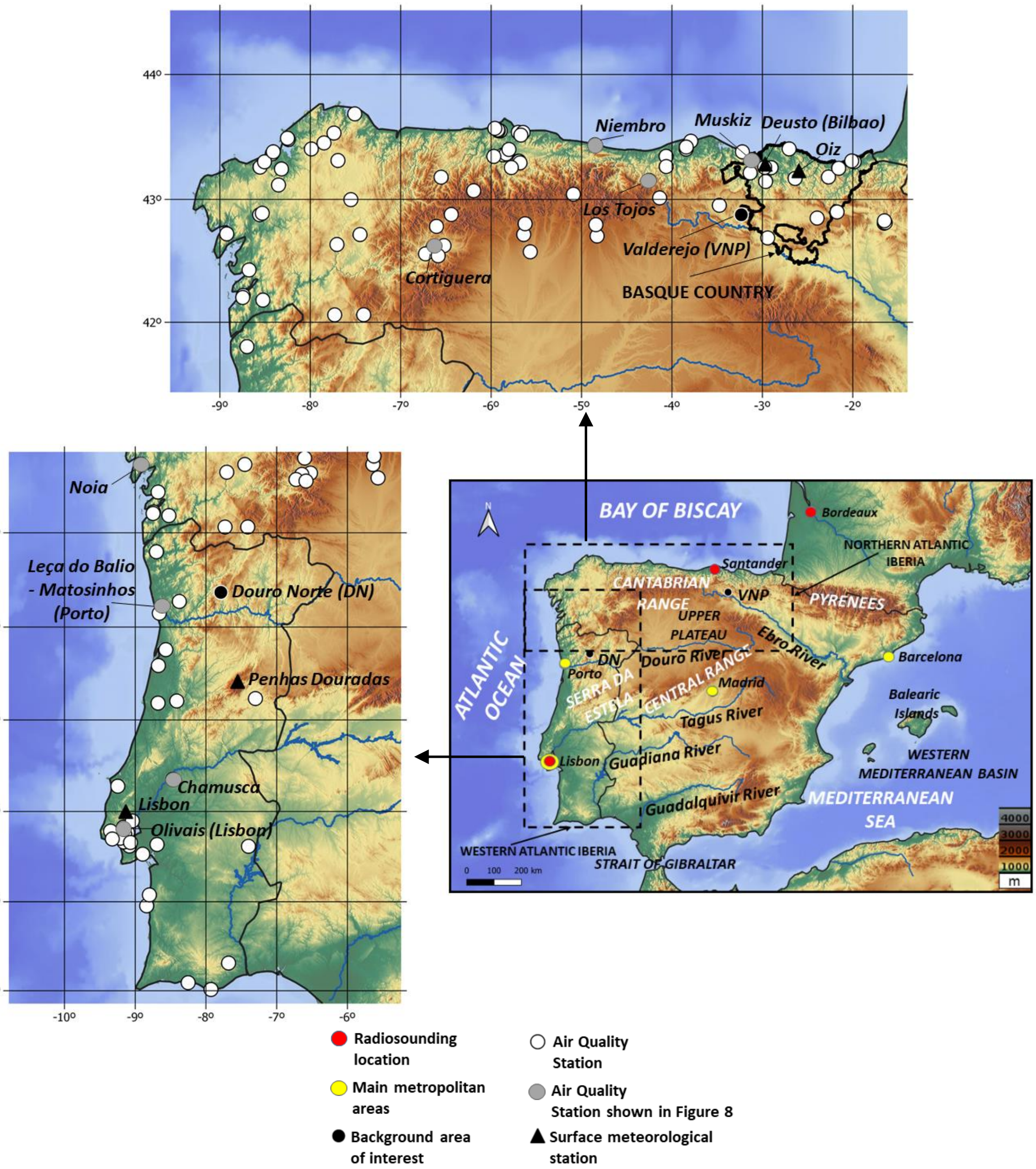

Figure 1. Topographic map of the Iberian Peninsula (bottom-right): The territory delimited to the left towards the Atlantic Ocean is Portugal, to its right Spain, and to the north of the Pyrenees, France. Upper detailed map: North Atlantic Iberia (NAI) and left detailed map: Western Atlantic Iberia (WAI).

Over the last years, the highest O_3 hourly averaged concentration registered in NAI and WAI have been continuously measured in rural mountainous areas such as Valderejo Natural Park (VNP) station, in the Basque Country (Spain), and Douro Norte (DN) station, in Alvão Natural Park (Portugal). In both stations, O_3 exceedances are numerous, and O_3 levels are affected by primary pollutants (volatile organic compounds (VOCs) and nitrogen oxides (NO_x)) emitted on their corresponding coastline, that are transported inland due to the sea breeze circulation. Besides the contribution of local sources, the concentration profiles reflect the influence of atmospheric transport on a synoptic or regional scale (Evtyugina et al., 2009; Carvalho et al., 2010; Monteiro et al., 2012; Borrego et al., 2013, 2016; de Blas et al., 2019; Gómez et al., 2020). All these studies have analyzed various O_3 episodes for specific regions of the Iberian Atlantic Coast. However, there is a lack of a common modeling and assessing methodology for the whole region. The mechanisms producing O_3 episodes occurring simultaneously in the two sub-regions (NAI and WAI) of the Iberian Atlantic Coast are still in the process of being further documented.

1.2. Objectives

The main objective of this paper is to analyze a tropospheric O_3 episode with a remarkable intensity over a large region, covering Northern Atlantic Iberia (NAI) and Western Atlantic Iberia (WAI), and to establish possible O_3 interregional pathways between these regions and with the rest of the Iberian Peninsula and the European continent. For this purpose, we have established a methodology based on high-resolution meteorological and photochemical modeling to analyze the surface concentration and vertical distribution of O_3. The presence of a permanent wind shear throughout the entire episode added special complexity and posed a challenge to the search for the origin of the observed O_3 impact and the selection of the most appropriate reduction policies.

This paper is organized as follows: Section 2 describes the methodology employed, containing 2 subsections. Section 2.1. refers to the modeling system used, and Section 2.2. the validation method. The results and discussion are presented in Section 3, divided into three subsections, analyzing the meteorology of the episode in 3.1, statistical evaluation in 3.2, and O_3 concentrations in 3.3. Finally, in Section 4 we detail the conclusions of this study.

2. Methodology

In recent years Chemical Transport Models (CTM) have been used to simulate and analyze short-duration pollution episodes in IP (Valverde et al., 2016; Escudero et al., 2019; Pay et al., 2019). The use of fine grids in models (with high horizontal spatial resolutions of 1-3 km) has given good results in environments with complex topography, where mesoscale processes become particularly relevant for the interpretation of the O_3 production, accumulation, transport, and decay (Jiménez et al., 2006; Monteiro et al., 2009). High horizontal spatial resolution is also especially recommended when describing O_3 variability in industrial and urban areas (Baldasano et al., 2011).

We have used a photochemical modeling system configuration, combining meteorological, emission, and photochemical simulations. Models' execution (for Initial and Boundary conditions, among others) and validation require a variety of experimental data, all of them described throughout this section. Model results have been processed in order to analyze and represent vertical cross sections of the atmosphere, and we have calculated integrated O_3 concentrations from near-surface atmospheric levels up to 2,500 m Above Ground Level (AGL), according to the atmospheric thickness above the surface at which O_3 accumulates (Querol et al., 2018).

2.1. Simulations

2.1.1. Meteorology

The meteorological parameters required for air quality simulations were obtained using the Weather Research and Forecasting model (WRF), version 3.9.1.1 (Skamarock et al., 2008), using a modeling period from July 26 to August 9, 2018. We defined 3 domains with different resolutions (Table 1) and Lambert Conformal projection, as shown in Figure 2, with the center of the coarser domain at 45°N and 2.5°W, and 50°N and 35°N as true latitudes for the projection. The first grid (d01) extension covers a large part of the European continent and Northern Africa with a 27 km horizontal resolution. This domain is intended to include large atmospheric circulations between the North Atlantic, the Mediterranean Sea, and Northern Africa. It also includes important sources of atmospheric emissions located along the English Channel (United Kingdom, Northern France, Belgium, and the Netherlands) and Northern Africa (Gangoiti et al., 2006a). The second domain (d02), with a resolution of 9 km, incorporates the entire Iberian Peninsula, the South of France, and the coast of Northern Africa. In this way, it can document the Atlantic fronts over the region, the summer anticyclones and associated mesoscale flows in the Western Mediterranean Basin (Gangoiti et al., 2001, 2006b) and the flows developing in the Strait of Gibraltar (in 't Veld et al., 2021; Massagué et al., 2021). We also included a third domain (d03), with a resolution of 3 km, covering the North of the Iberian Peninsula and the South of France, so that atmospheric flows developed over the Ebro and the Douro Valleys could be represented with an adequate detail. This third domain includes areas of special interest with O_3 measuring reference stations for the analysis of interregional O_3 transport (Navazo et al., 2008; de Blas et al., 2019; Gómez et al., 2020). We used 31 η layers covering up to approximately 15,500 m AGL. The vertical resolution near the boundary layer, at the surface, is greater than at higher levels, where the distance between layers increases (Table S1).

Table 1. Spatial characteristics of the domains used in WRF and CAMx.

Domain	Spatial Resolution	WRF Number of cells	CAMx Number of cells
d01	27 km x 27 km	162 x 162	160 x 160
d02	9 km x 9 km	195 x 150	193 x 148
d03	3 km x 3 km	393 x 186	389 x 182

The physical parameterizations of the meteorological model are determinants when simulating air quality. In this study, we proposed a configuration already used by other studies in IP with satisfactory results (Borge et al., 2014; Escudero et al., 2019). Other studies, also carried out in IP (Pay et al., 2010; Borrego et al., 2013; Banks and Baldasano, 2016), have used similar parameterizations with changes in the configuration of the Planet Boundary Layer (PBL). The selected parameterization is shown in Table S2. It is mainly based on the configuration of Borge et al. (2008) modifying the longwave radiation scheme by the Rapid Radiative Transfer Model (RRTM) (Mlawer et al., 1997) recommended by the WRF developers. Additionally, Sea Surface Temperature (SST) supplied by NOAA has been used, specifically Optimum Interpolation SST (https://www.ncei.noaa.gov/products/optimum-interpolation-sst), with a spatial resolution of 0.25° x 0.25° and a daily temporal resolution (Banzon et al., 2016).

Initial and boundary conditions were generated using 6 h reanalysis from the European Centre for Medium-Range Weather Forecasts (ECMWF), specifically, ERA-Interim reanalysis global data (Berrisford et al., 2011) of 0.75° x 0.75° horizontal resolution. Its vertical resolution is higher near the surface (every 25 hPa from 1,000 hPa to 700 hPa), decreasing for higher levels. We also used the same data for Four-Dimensional Data Assimilation (FDDA) above the PBL in the coarser domain (d01).

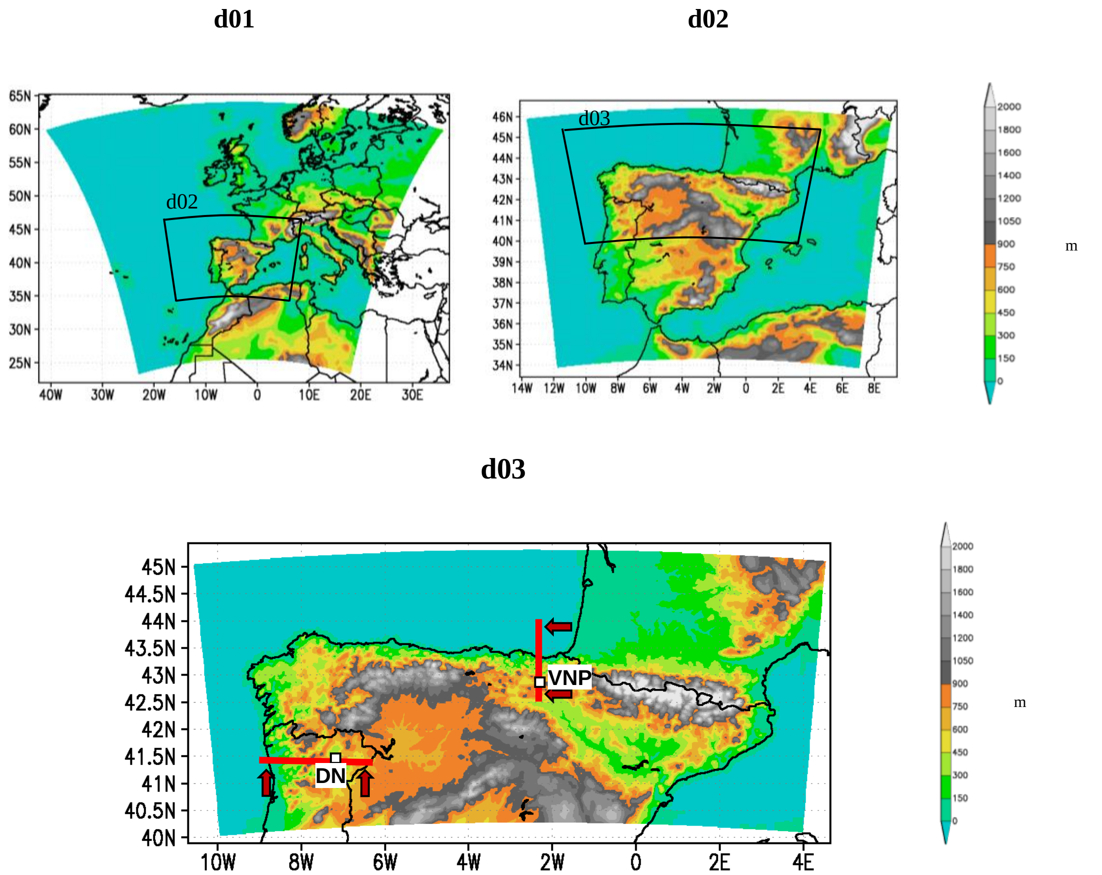

Figure 2. Domains used for the meteorological and photochemical simulations on its topographic map: d01 (27 km) -Europe and North Africa, d02 (9 km) - Iberian Peninsula-, d03 (3 km) -Northern Iberian Peninsula-. Red lines: location and extent of atmospheric vertical cross-sections analyzed in VNP and DN.

2.1.2. Photochemistry and dispersion

We used the Comprehensive Air Quality Model with Extensions (CAMx), version 6.50 (Ramboll Environment and Health, 2018). The domain and horizontal resolution selected for this air quality model were identical to those used for WRF model (see Table 1). We used 14 σ layers going up to approximately 4,800 m AGL with the first layer being approximately 20 m thick. Concentrations were calculated at the midpoint of each layer, so the modeled values of the first layer corresponding to a height of approximately 10 m AGL, and the same applies to other layers. The different thicknesses of the layers and their correspondence with WRF layers are shown in Table S3.

The gas-phase mechanism CB6r4 was used in this work (Ramboll Environment and Health, 2018). For inorganic thermodynamics and gas-aerosol partitioning CAMx uses ISORROPIA (Nenes et al., 1998, 1999) and for dry deposition we chose the algorithm of Zhang et al. (2001, 2003). The O_3 column data was obtained from the O_3 Monitoring Instrument (OMI) of NASA's Total O_3 Mapping Spectrometer (TOMS) satellite, which has a daily temporal resolution and a horizontal spatial resolution of 1° x 1° (available at https://acd-ext.gsfc.nasa.gov/anonftp/toms/omi/data/ozone/). O_3 column data were used in the Tropospheric Ultraviolet and Visible (TUV) radiation and photolysis model used by CAMx: Dr. Madronich's preprocessor for CAMx calculates the photolysis rates for clear skies, and then CAMx internally adjusts these rates in case of clouds or aerosols (NCAR, 2011). The initial and boundary conditions for the first domain (d01) were obtained from the global air quality model CESM2.1: CAM-Chem (Lamarque et al., 2012). We first ran the first domain (d01), and for the other two (d02 and d03) we used BNDEXT CAMx preprocessing program to generate initial and boundary conditions extracted from d01. In the first simulation for d01, we extracted the following simulated pollutants' concentrations to generate d02's initial and boundary conditions: O_3, NO, NO_2, SO_2, $OH^\bullet$, $HO_2^\bullet$, H_2O_2 (hydrogen peroxide), CO, CH_4, Ethane, Ethene, Ethyne, Propane, Formaldehyde, Isoprene, Monoterpenes, Benzene, Toluene and other monoalkyl aromatics, Xylene and other polyalkyl aromatics, HNO_3, HONO (nitrous acid), PAN (Peroxyacil Nitrate), and $NO_3^\bullet$.

The CAMx domain configuration was the same as that used in WRF (Figure 2) and the type of projection, their central points, and reference latitudes. However, a slight reduction of dimensions was necessary for its correct usability in CAMx, due to the way CAMx domains are configured and to the limitation imposed by some emission models such as MEGAN. Also, for CAMx to properly solve the boundary conditions of the nested domains, some cells, denominated as buffer cells, were added at the outer edges around the perimeter of each domain.

CAMx incorporates the WRFCAMX preprocessor, version 4.6, which transforms the WRF meteorological variable fields into the specific meteorological variables required by CAMx. We chose to run this program with the YSU scheme of the PBL (Hong, Noh, and Dudhia, 2006) to be consistent with the PBL configuration used in WRF.

2.1.3. Emissions

We used the Model of Emissions of Gases and Aerosols from Nature (MEGAN) (Guenther et al., 2006; Guenther et al., 2012), an empirical model of biogenic emissions most widely used by the scientific community for the calculation of VOCs from vegetation (Sindelarova et al., 2014). The new version (MEGAN 3.0) includes for the first time a processor for calculating Emission Factors (EF) for different species, where the user may incorporate custom high spatial resolution EF databases from specific vegetation data. This processor contains a wide selection of EFs for more than 42,500 species types based on the available databases (Guenther, 2017).

MEGAN requires as input for the biogenic emissions estimation for the different domains used in the CAMx simulation a meteorological simulation, a Leaf Area Index (LAI) spatial distribution, and EF spatial distributions. We incorporated meteorological data calculated by WRF into MEGAN 3.0 through the Meteorology-Chemistry Interface Processor (MCIP) tool (Otte and Pleim, 2010), using the preprocessors included in this new version of MEGAN to calculate EF, but we improved it by updating Spanish land use and vegetation maps databases from the National Forest Inventory (Torre-Pascual et al., 2021). Of the existing global LAI products, we chose the one generated by the MOderate resolution Imaging Spectroradiometer (MODIS) instrument of NASA's Aqua and Terra satellites (Myneni et al., 2002; Yang et al., 2006). The wide use of this product is due to its high spatial resolution (1 km x 1 km), temporal resolution (every 8 days) and its frequent updating (Yuan et al., 2011). However, the instrument shows uncertainties due to cloudiness and seasonal snow cover, and current MODIS LAI products are spatially and temporally discontinuous and inconsistent (Zuazo et al., 2023). Thus, we used the 2010 reprocessed MODIS LAI by Yuan et al. (2011), instead of the one for 2018 because it was not available at the time of this study.

We used the Emission Database for Global Atmospheric Research (EDGAR) global anthropogenic emission inventory (Crippa et al., 2018), in its version 4.3.2, published in December 2017. EDGAR contains anthropogenic emissions from the European and African continents, which fit the extension of the main domain (d01) with a high spatial (0.1° x 0.1°) and temporal resolution (monthly averages for 2010) for the whole area. We selected the most relevant compounds for the analysis of tropospheric O_3 pollution episodes, specifically: CO, NH_3, Non-Methane Volatile Organic Compounds (NMVOC), NO_x, SO_2, and CH_4. Emissions due to aviation have been excluded, except for landings and take-offs, as they do not originate near the surface and can be expected to have little influence on surface and near-surface O_3. We used the SPECIATE tool (EPA, 2016) to speciate NO_x and NMVOC.

Emissions in EDGAR's inventory are classified according to their origin following the Convention on Long-Range Transboundary Air Pollution (CLRTAP) - Nomenclature for Reporting (NFR) sectors (Janssens-Maenhout et al., 2019). We performed the daily and hourly temporal distribution of emissions using the temporal distribution coefficients used in the LOTOS-EUROS CTM (Denier van der Gon et al., 2011). LOTOS-EUROS temporal profiles were defined for SNAP (Selected Nomenclature for Sources of Air Pollution) sectors contemplated in the CORINAIR/EMEP methodology (EEA, 2016). Therefore, we regrouped the latter sectors based on the NFR-SNAP mapping table (https://www.ceip.at/fileadmin/inhalte/ceip/00_pdf_other/nfr09_snap_gnfr.pdf). We used the Sparse Matrix Operator Kernel Emission model (SMOKE) (https://www.cmascenter.org/smoke/) for spatial disaggregation and adaptation for the domains, temporal disaggregation, and pollutant speciation.

2.2. Validation

To validate the WRF-CAMx simulation, we combined the analysis of the modeling results with the assessment of meteorological reanalysis, in particular ERA5 reanalysis, meteorological observations, and O_3 measured concentrations. This allowed us to verify the model's performance with experimental data, not only at the surface level but also at upper levels. For comparison with experimental data, we have preferentially taken the higher spatial resolution outputs of the simulations.

2.2.1. ERA5 hourly reanalysis

We have taken as a reference for validating the meteorological simulation the ERA5 reanalysis. ECMWF released a new, improved meteorological reanalysis, namely ERA5 (Copernicus Climate Change Service, 2018; Hersbach et al., 2020), with a higher spatial resolution (0.25° x 0.25°) and higher temporal resolution (hourly) than ERA-Interim. Due to the difficulty in collecting meteorological observation data and the unreliability of some of the data found, we have decided to use ERA5 reanalysis as a main reference, in addition to the selection of 4 meteorological stations that we mention afterward, since it incorporates most of the official meteorological measurements made for this region. We have compared ERA5 surface temperature and winds (surface and 750 hPa) with the WRF simulation. With all this information, we have performed qualitative comparisons for a proper understanding of the episode. In addition, we have examined the visible channel images from the Meteosat satellite, available on NOAA's Global ISCCP B1 Browse System (Knapp, 2008), shown in Figure S1, for evaluating cloudiness and the synoptic evolution during the episode.

2.2.2. Surface and upper air meteorological observations

Among the meteorological observational data, we have compared radiosonde data from Lisbon, Santander, and Bordeaux (locations shown in Figure 1) with the WRF simulation, allowing us to evaluate the atmospheric evolution at different altitudes throughout the episode. We gathered radiosonde data from the database of the University of Wyoming (http://weather.uwyo.edu/upperair/bufrraob.shtml), as it has an extensive compilation of all radiosoundings conducted globally.

We compiled surface observations data from two stations of the Basque Meteorological Network (EUSKALMET), one of them located in Bilbao (Deusto) at sea level, and another one in Oiz, at 998 m ASL (Figure 1). For Portugal, we collected two stations' data from the Global Hourly - Integrated Surface Database (ISD) of the NCEI (https://www.ncei.noaa.gov/products/land-based-station/integrated-surface-database), one in Lisbon, at sea level, and Penhas Douradas, at 1,398 m ASL.

2.2.3. Surface O_3 measurements

To analyze air quality in the IP study area, we used surface observation data of hourly O_3 concentrations for Spain and Portugal. The database from Spain is available at MITECO Ministry's website (https://www.miteco.gob.es/es/calidad-y-evaluacion-ambiental/temas/atmosfera-y-calidad-del-aire/calidad-del-aire/evaluacion-datos/datos/Datos_oficiales_2018.aspx) which groups all the data from the air quality networks of the Autonomous Communities, and those for Portugal from its Air Quality Network (https://qualar.apambiente.pt/) provided by the Agência Portuguesa do Ambiente. For the statistical analysis of the two regions analyzed in this paper, we have selected the stations in NAI from the Spanish database shown in Figure 1, and for WAI all the stations from the Portuguese database.

2.2.4. Statistical evaluation of simulated O_3 concentrations

The uncertainty associated with the models is determined by comparing the experimental data (measurements) and the results of their simulations. Several studies have developed different methodologies and there is currently no standardized methodology for this purpose (Borrego et al., 2008). In recent years, the use of a series of statistical indicators has prevailed in the scientific literature (Bessagnet et al., 2016; Oikonomakis et al., 2018). In this work, we have chosen to use a set of metrics commonly employed by the aforementioned studies described in Table 2. This has allowed us to compare the metrics used here with the work of other authors. We carried out this evaluation for the selected stations shown in Figure 1 for NAI and WAI, also shown with their coordinates in Tables S4 and S5.

Table 2. Statistical metrics used for the photochemical simulation.

Statistical metrics	Equation
Mean Bias (MB)	$\frac{1}{N}\sum_{i=1}^{N}(Model_i - Obs_i)$
Mean Error (ME)	$\frac{1}{N}\sum_{i=1}^{N}\lvert Model_i - Obs_i\rvert$
Normalized Mean Bias (NMB)	$\frac{\sum_{i=1}^{N}(Model_i - Obs_i)}{\sum_{i=1}^{N} Obs_i}$
Index of Agreement (IOA)	$1 - \frac{N \cdot \mathrm{RMSE}^2}{\sum_{i=1}^{N}(\lvert Model_i - \overline{Obs}\rvert + \lvert Obs_i - \overline{Obs}\rvert)^2}$
Pearson correlation coefficient (r)	$\frac{\sum_{i=1}^{N}(Model_i - \overline{Model}) \cdot (Obs_i - \overline{Obs})}{\sqrt{\sum_{i=1}^{N}(Model_i - \overline{Model})^2} \cdot \sqrt{\sum_{i=1}^{N}(Obs_i - \overline{Obs})^2}}$

3. Results and discussion

First, we have evaluated the results of the meteorological model as they determine the performance of the photochemical model. Secondly, we have assessed the performance of the simulated O_3 concentrations by CAMx with its statistical analysis, contrasting with observations. At the end of this section, we have analyzed the evolution of the episode from CAMx results and observations of O_3 concentrations.

3.1. Meteorology

The six-hourly NCEP Climate Forecast System Reanalysis (CFSR) historical archive in Wetterzentrale (http://www.wetterzentrale.de/) and the ERA5 reanalysis are used to describe the synoptic meteorology. Surface and upper air meteorological observations of a set of stations (section 2.2) are also discussed in this section in the context of the different scales of the meteorological processes working together during the episode and the eventual adequacy of the response of the WRF model to the observed meteorology.

3.1.1. Synoptic analysis and upper-level winds

Following the NOAA NCEP Climate Forecast System Reanalysis (CFSR) (Saha et al., 2014), the synoptic conditions during the O_3 episode (2-6 August) (Figure 3) were characterized by a large upper-level ridge which extended from northern Africa to western Europe crossing the Iberian Peninsula and an associated large area of surface high-pressures. The surface anticyclone covered the whole European Atlantic coast from Scandinavia to Iberia. This pressure distribution is compatible with East to Northeasterly winds at surface levels following the coast along the European Atlantic, and warm southerlies at upper levels over IP, which bring vertical stability and the adequate conditions to O_3 episodes ("accumulation periods") in central Iberia (Querol et al., 2018). The easterly winds in the marine boundary layer of the northern coast of Spain and the sea-breeze inland convergences are behind most of the O_3 episodes in the Basque Country (Gangoiti et al., 2006a). These episodes, though less intense, occurred even during the COVID-19 lockdown period after a significant reduction of anthropogenic precursors (Gangoiti et al., 2021), and they were attributed to O_3 importation across southern France and the Bay of Biscay.

The ERA5 reanalysis at the surface and upper levels shows a more detailed wind field distribution and time evolution during the initiation of the episode (Figure S2). Easterly winds in the Bay of Biscay and the northerlies at the coast of Portugal (Figure S2 a.1 and b.1) in the marine boundary layer were decoupled from the relatively warm winds at upper levels (Figure S2 a.2 and b.2). That air mass circulated anticyclonically around IP, a fact that could hardly be inferred from the CFS Reanalysis in Figure 3, forcing moderate southerlies over WAI, weak westerlies over NAI, and almost calm conditions over the SW coast of France on August 2 (Figure S2 a.2). That meant a maximum wind directional shear of 180º in both WAI and NAI regions. This type of upper-air anticyclonic circulations seems to be a key component of the Northern African middle troposphere wind regime, which is behind the desert dust transport accumulation and redistribution in the region (Gangoiti et al., 2006b). From August 3 onwards, there was a change in the wind field at upper levels, registered by the ERA5 reanalysis: the warm air mass circulating at upper levels moved to the west, and the wind turned to the N over the eastern half of IP. That changed completely the atmospheric circulation at those levels, being opened to the entry of air masses of European origin to NAI, while the circulation pattern remained from the south over a larger part of the coastal WAI and from the NE over Southern Portugal (Figure S2 b.2). However, these changes were not observed at surface level: at the Atlantic coast of Iberia surface winds did not show significant changes from the previous day (Figure S2 b.1). The new wind configuration at surface and upper levels over WAI, which lasted for the rest of the O_3 episode, was more similar to those described in Gangoiti et al. (2006a) and Valdenebro et al. (2011) for the northern coast.

The end of the episode started on August 6 with the development of an upper-level trough associated with a mid-latitude depression to the south of Iceland (Figure 3). The trough, marked with a black arrow in the figure, extended to NW Iberia and forced a surface (and upper level) cold air mass advection from the north-west with a frontal region (dashed line in Figure 3), which crossed NAI and WAI during the following 24 hours. The ERA5 wind and temperature data in Figure S3 shows the observed changes during the frontal passage: the west and northwesterly wind advection started on August 6 (Figure S3 a.1 and a.2) and moved to the west during the following day, with westerlies at the surface and intense south-westerlies at upper levels (Figure S3 b.1 and b.2). A similar wind field distribution has been estimated by the WRF simulation during the whole episode, both at surface and upper levels, shown in Section 3.3. in the context of the simulated inter-regional O_3 transport and distribution.

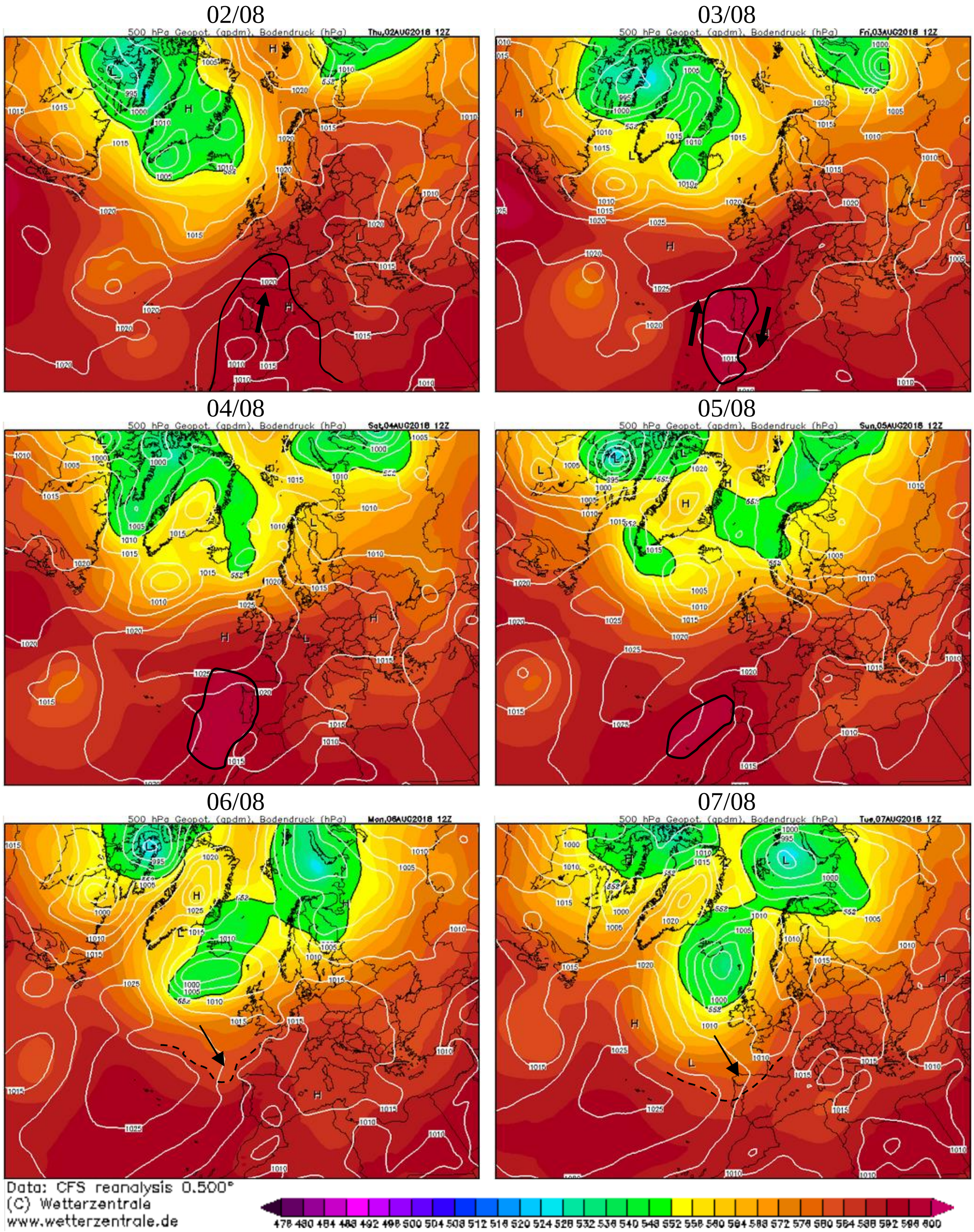

Figure 3. Synoptic conditions during the O_3 episode with geopotential height at 500 hPa (geopotential dm, shaded) and surface pressure (hPa, contours) during the period of the high ozone episode (August 1-7). L and H mean "low pressure centre" and "high pressure centre" respectively. Continuous black lines represent the warmer air mass over the IP and dashed black lines represent the Atlantic advection. Source: NCEP CFS reanalysis from www.wetterzentrale.de.

Radiosonde wind data and WRF simulated vertical profiles at three sounding sites (Lisbon, Santander, and Bordeaux) of WAI and NAI are represented in Figure 4 for the "extended" O_3 episode (1-8 August). Observations (left) and modeled vertical winds (right) agree and correspond with the surface and upper air wind field reanalysis described above. During the initiation of the episode (1-2 August) southerly winds (SW at Santander and Bordeaux, SE in Lisbon) blew above 1,500-2,000 m ASL, decoupled from the easterlies at the surface (below 1,000-1,500 m ASL). The following changes in the wind field at upper levels, registered by the reanalysis during the period 3-6 August, are represented by the northerlies above

1500-2000 m ASL (Santander and Bordeaux) and the easterlies backing to the north (Lisbon), depicted in Figure 4. These changes correspond to the westward displacement of the anticyclonic circulation at upper levels. The cold front passage at the end of the episode is represented in Figure 4 by the surface north-westerlies backing to the SW with height, initiated during the afternoon of August 6 in Lisbon and Santander, and on August 7 in Bordeaux.

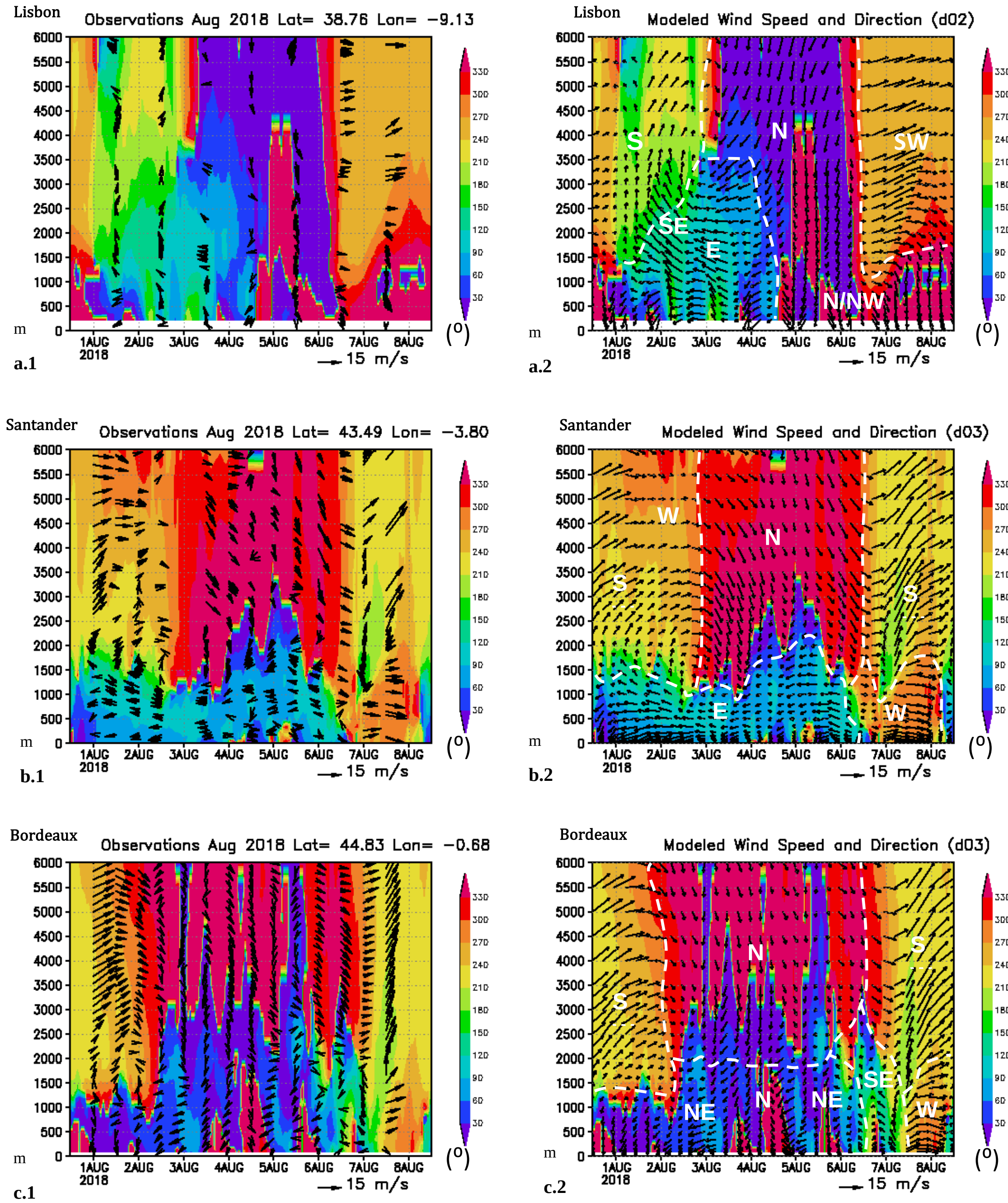

Figure 4. Wind vectors measured in radiosonde (left) and WRF simulations (right) for the period 01-08 August 2018. The range of colors in all graphics represents the simulated wind direction. The size of the vectors represents wind speed.

3.1.2. Surface temperature and winds

Figures S4 and S5 show the sequence of temperatures and wind observations (red) and WRF simulations (blue) at the two selected surface meteorological stations in NAI during the extended O_3 episode (1-8 August). They document the meteorological conditions at a sea-level coastal station (Deusto) and at an elevated inland site (mount Oiz). Deusto is located in the city of Bilbao, in a coastal valley with SE-NW orientation, draining directly into the sea along a 10-km-long estuary. Thus, the land-sea breeze regime at this station is represented with successive channeled land (S and SE) and sea (N-NW) daily wind cycles (Figure S4). We have observed a pronounced diurnal variability in observed wind speed compared with the model, this difference may affect the extent of the simulated emitted O_3 precursors' dispersion with these wind cycles. The coastal convergence contrasts with the meteorological conditions at the inland station (Figure S5), which was not affected by sea breeze regimes. The wind sequence in mount Oiz is more similar to the upper air observations at around 1,000 m ASL over the Santander sounding site (Figure 4), located 100 km to the west in the northern coast. The simulations follow main temperature and wind shifts during the episode in both stations. Two main changes can be distinguished in Figure S5. (1) During the first day of the episode, the south-easterly winds changed to the north-east, concurrent with the observed changes in the upper-level anticyclonic circulation described above and persisted during the rest of the O_3 episode. The simultaneous documented convergence of the coastal sea-breeze regimes shown in Figure S4 (transporting local emissions) together with the E-W transport, in the marine boundary layer of O_3 and precursors originated further away to the East was responsible for the observed O_3 concentrations in the inland monitors during that period, as discussed in the next section. (2) During the last day of the episode (August 6), intense south-westerly prefrontals preceded the arrival of the cold front (NW in Figure S5) at the end of the day in mount Oiz. Those warm (30 ºC) offshore prefrontals, registered at mount Oiz at around 1,000 m ASL, rose the temperature at the coastal stations (37 ºC in Deusto at midday), when the upper-level southerlies were coupled with the surface winds at the lee of the coastal mountain ranges, as it was the case during that foehn episode in the Basque Coast. Attending to the coastal station records (Figure S4), the sea breeze could develop against the offshore winds during the afternoon, while the prefrontal south-westerlies still kept blowing above the coastal sea breeze and on top of the inland mountain stations, as mount Oiz (Figure S5).

Figures S6 and S7 show a similar sequence (as in Figures S4 and S5) of temperatures and wind observations-simulations in two meteorological surface stations in WAI. Similar to the NAI site selection, they document the meteorological conditions at a sea-level coastal station (Lisbon) and at an elevated inland site (Penhas Douradas, 1,398 m ASL). The simulations also follow the main temperature and wind shifts during the period in both stations. The land-sea breeze regime in Lisbon was represented with successive land (E and NE) and sea (NW) daily wind cycles (Figure S6). As for the case of the NAI stations, the sites showed a completely different behavior, mainly due to the observed decoupling between the upper and lower-level flows. Sea breeze cycles were observed at the coastal station in Figure S6, which persist during the whole episode. On the contrary, initial south-easterly winds in Penhas Douradas (Figure S7), in agreement with the upper-level anticyclonic circulation, changed to the north and north-west, according to the observed synoptic changes (Figure S2) and the vertical soundings in Lisbon (Figure 4) between 1,000-1,500 m ASL. During the last day of the episode (August 6), a temperature decrease of 10-15 ºC and intense and persistent northwesterly winds (without cycles) in both stations (Figures S6 and S7) marked the cold front advection before midday, preceding the changes observed in the NAI stations.

3.2. Statistical evaluation of simulated O_3 concentrations

We have calculated the statistical metrics shown in Table 2 for 116 O_3 measurement stations for the period from August 1 to 7. All these stations meet the criterion of data availability of more than 95% of hourly O_3 concentrations. Of the total number of stations, 83 are located in Spain, in NAI, and the remaining 33 are located in Portugal, in WAI. The dispersion of the individual metrics is shown in Figure S8. The median Pearson correlation coefficient (r) for all the stations was 0.66 and the median Index of Agreement (IOA) was 0.70. The CAMx model tends to overestimate O_3 concentrations for this region, as shown by the box and whisker plots of the Mean Bias (MB): the interquartile values, from the 25th percentile to the 75th percentile, are all positive. The median Mean Bias (MB) is +14.0 $\mu g \cdot m^{-3}$ and the median Mean Error (ME) is 24.0 $\mu g \cdot m^{-3}$. The calculated statistical parameters are within the range of values found in similar studies.

Statistical metrics calculated for each site are represented in Figure 5 and shown in Table S4 and Table S5. We have detected better model performance at WAI, where median r was 0.74 and IOA was 0.79, compared to 0.62 and 0.66, respectively, for the NAI stations. The same is true for the median MB values: -1.0 $\mu g \cdot m^{-3}$ versus +20.0 $\mu g \cdot m^{-3}$, and with a median ME of 20.0 $\mu g \cdot m^{-3}$ versus 26.0 $\mu g \cdot m^{-3}$ at WAI and NAI, respectively. This statistical difference could be due to an over-representation of some areas due to the proximity of measurement stations in NAI, and to the number of industrial stations that are exposed to industrial emission sources.

In WAI, three stations are highlighted as having a poor model performance: the urban background PT01044 (Paços de Ferreira, Porto) in the North, and the suburban industrial PT04001 (Monte Chãos) and rural background PT04002 (Monte Velho), in the southwest of Portugal. Paços de Ferreira municipality stands out due to its furniture and textile industry. The largest positive Mean Bias error (+68 $\mu g \cdot m^{-3}$) calculated for this area indicates that the model is strongly overestimating O_3 concentrations, which may be due to unrealistic NO_x emissions such as lack of local NO emissions in the model, affecting the modelled O_3 concentrations through the underestimation of the NO_x titration process. Although Monte Chãos and Monte Velho are both located near the Sines Industrial and Logistics Zone, the largest industrial area in Portugal, other factors than industrial emissions may be playing a crucial role in the modelling performance: a large forest fire took place in Monchique, from the 3rd to the 10th of August, burning around 27,000 hectares of forest and agricultural land, emitting a huge amount of pollutants, and thus affecting air quality. On the contrary, the rural background PT01048 (Douro Norte), in the North, exhibits the best statistical metrics, with IOA=0.88 and ME= 10 $\mu g \cdot m^{-3}$.

In NAI, the rural background ES1599A (Pagoeta) and the urban background ES1747A (Rotxapea), both located at the Eastern part of NAI, have the best performance, with IOA= 0.86 and 0.83, respectively. The overall behavior of the statistical data in this area exhibits a strong correlation, with high IOA and r values, albeit with a general overestimation of O_3 levels. Stations in NAI might lack representativeness for background O_3 measurements since many of them are located near industrial centers with high NO_x emissions and there are few background stations that provide useful and reliable data to address O_3 transport and accumulation processes.

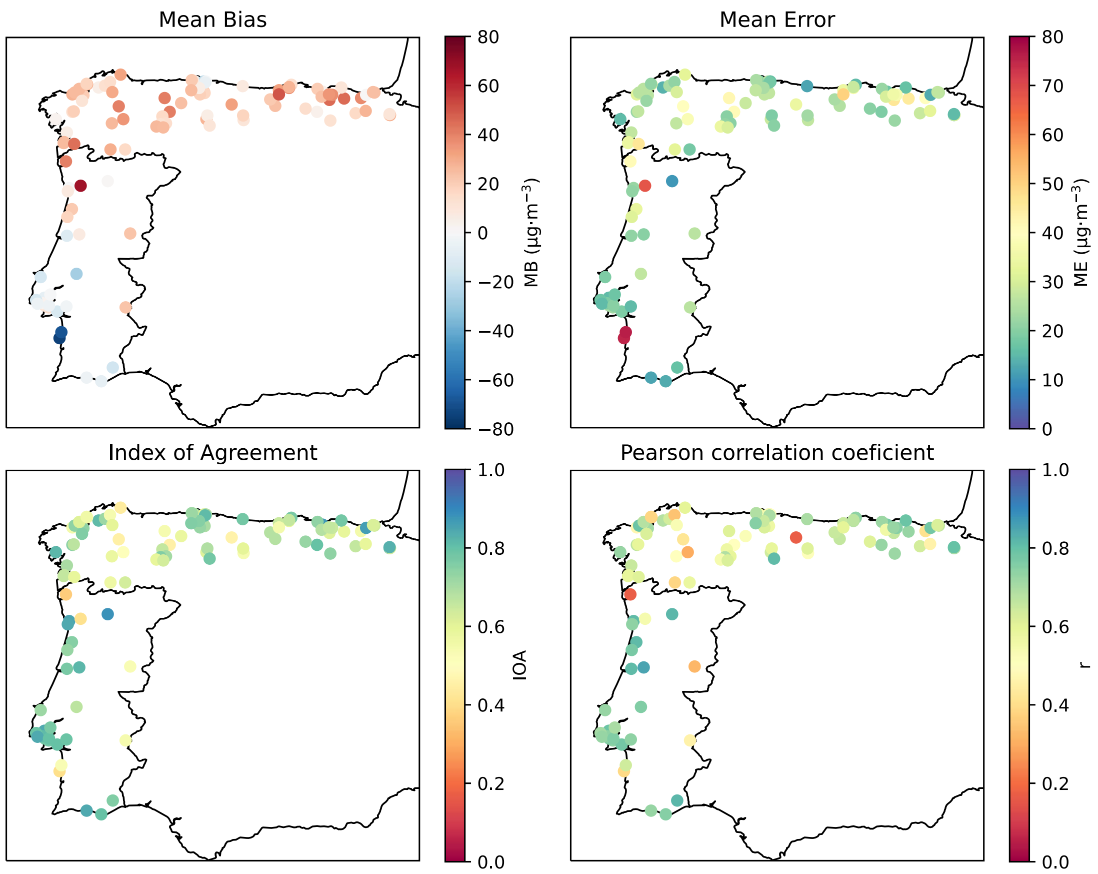

Figure 5. Spatial distribution of the values of the Mean Bias (MB), Mean Error (ME), Index of Agreement (IOA), and Pearson correlation coefficient (r).

For every hourly interval, we computed the average O_3 concentrations of observed and simulated data across all 116 stations within the domain. This allowed us to determine the overall average O_3 concentration across all sites in the domain (Figure 6). While this process involved pairing data temporally, it did not differentiate spatial distribution. The graphical representation demonstrates that WRF-CAMx generally replicates the daily O_3 patterns well and overestimates the lowest observed concentrations, particularly during nighttime in this specific episode. Our assessment reveals the model's ability to capture the initial sudden rise in O_3 concentrations, both of which depict an increase of approximately +25-30 $\mu g \cdot m^{-3}$ in maximum concentrations compared to the preceding day on August 2. During the following days, maximum values persist consistently above 120 $\mu g \cdot m^{-3}$. The decline observed on August 7 is also well replicated along with the dissipation of the episode. Despite nighttime discrepancies, our evaluation suggests that the model's application remains suitable for the objectives of our research.

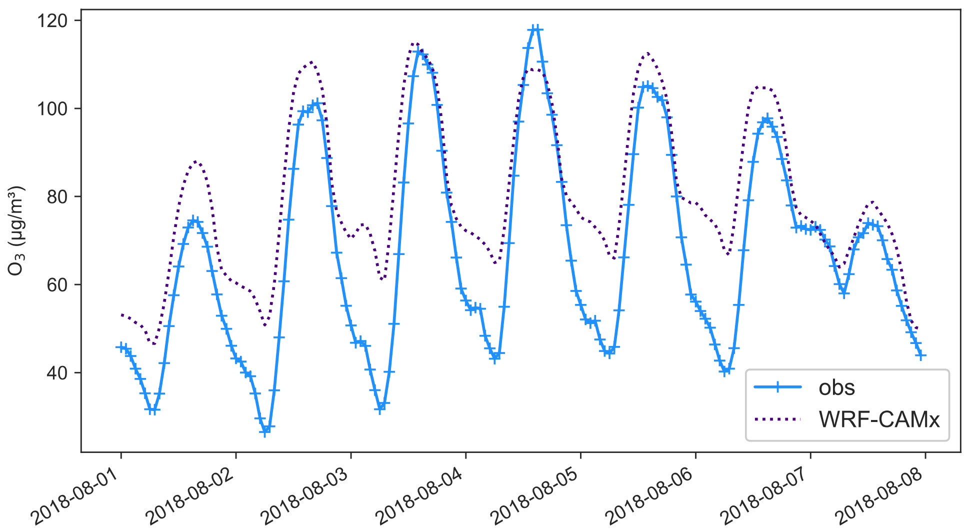

Figure 6. Time series plot of modelled and observed O_3 average concentrations in the 116 sites considered, between August 1 and 7, 2018 (average concentrations considering pairing in time but not pairing in space).

3.3. O_3 concentrations

This section presents an analysis of the observed and simulated O_3 surface concentrations and their integrated concentrations up to 2,500 m AGL. We have also analyzed two vertical cross-sections (red lines in Figure 2) of the atmosphere in the areas of interest of the Valderejo Natural Park (VNP) and Douro Norte (DN), which have shown some of the main O_3 transport pathways in these inland areas where large exceedances occur.

The evolution of the episode is shown in Figure 7 and Table 3. From July 31 to August 8, O_3 concentrations exceedances in the Iberian Peninsula were numerous (Figure 7), with high concentrations every day in Madrid and Barcelona metropolitan areas. The days with the highest number of measurement stations exceeding the European Directive target value and the information threshold occurred from August 2 to 6, particularly in the Atlantic Coast of IP (Table 3), where there was a notable increase in concentrations (Figure 7).

The initiation phase of the episode on the Atlantic Coast of IP began on August 2. It was characterized by an O_3 maximum hourly concentration increase of more than 40 $\mu g \cdot m^{-3}$ in Portugal (see Chamusca and Noia stations in Figure 8) and more than 30 $\mu g \cdot m^{-3}$ in non-coastal areas of NAI (see Valderejo and Los Tojos stations in Figure 8). That increase was due to a fumigation described in Section 3.3.1. On August 3 the highest number of exceedances of the European Directive occurred in NAI, marking the beginning of the peak phase: 38 stations exceeded the target value and 11 exceeded the information threshold (Table 3). During that second day, O_3 concentrations increased again by more than 30 $\mu g \cdot m^{-3}$ (Figure 8), with notable increases in DN and VNP of more than 60 $\mu g \cdot m^{-3}$, reaching maximum hourly concentrations of more than 180 µg·m-3. These increases coincided with the beginning of inflows of European continental air masses into IP with northerly winds. Hourly concentrations above 120 $\mu g \cdot m^{-3}$ were exceeded daily during this peak phase, extended until August 5.

On August 6, the dissipation phase began in WAI, but not in NAI, particularly in its coastal areas due to the foehn effect described in Section 3.1.2. Finally, on August 7, all concentrations dropped significantly due to the Atlantic advection. The detailed analysis of the phases with the simulated O_3 concentrations is shown below.

Table 3. Number of air quality monitoring stations within Portugal and Spain and the Atlantic Coast in which the European Directive O_3 target value and information threshold are exceeded, between July 31 and August 08, 2018.

Air quality monitoring stations: Portugal and Spain									
	31.07	01.08	02.08	03.08	04.08	05.08	06.08	07.08	08.08
Number of stations where max 8h-mean concentrations > 120 $\mu g \cdot m^{-3}$	53	79	125	146	164	203	170	75	31
Number of stations where max 1h-mean concentrations > 180 $\mu g \cdot m^{-3}$	2	12	7	14	20	9	3	1	0
Air quality monitoring stations: Atlantic Coast									
Number of stations where max 8h-mean concentrations > 120 $\mu g \cdot m^{-3}$	0	1	27	38	31	23	16	3	0
Number of stations where max 1h-mean concentrations > 180 $\mu g \cdot m^{-3}$	0	1	4	11	13	2	0	1	0

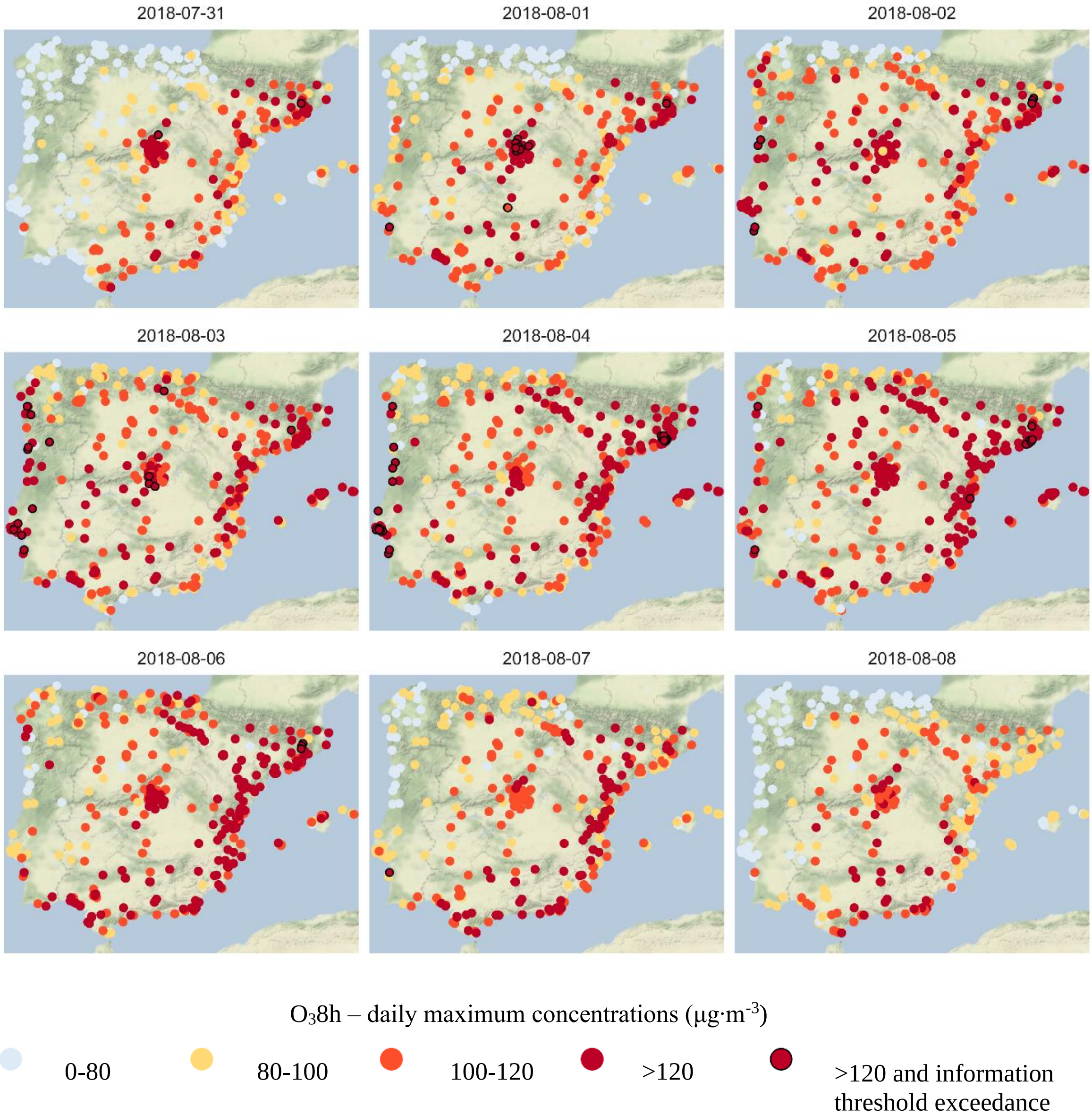

525 **Figure 7. Daily evolution of the spatial distribution of maximum daily 8-hour O_3 concentrations, from July 31 to August 8.**

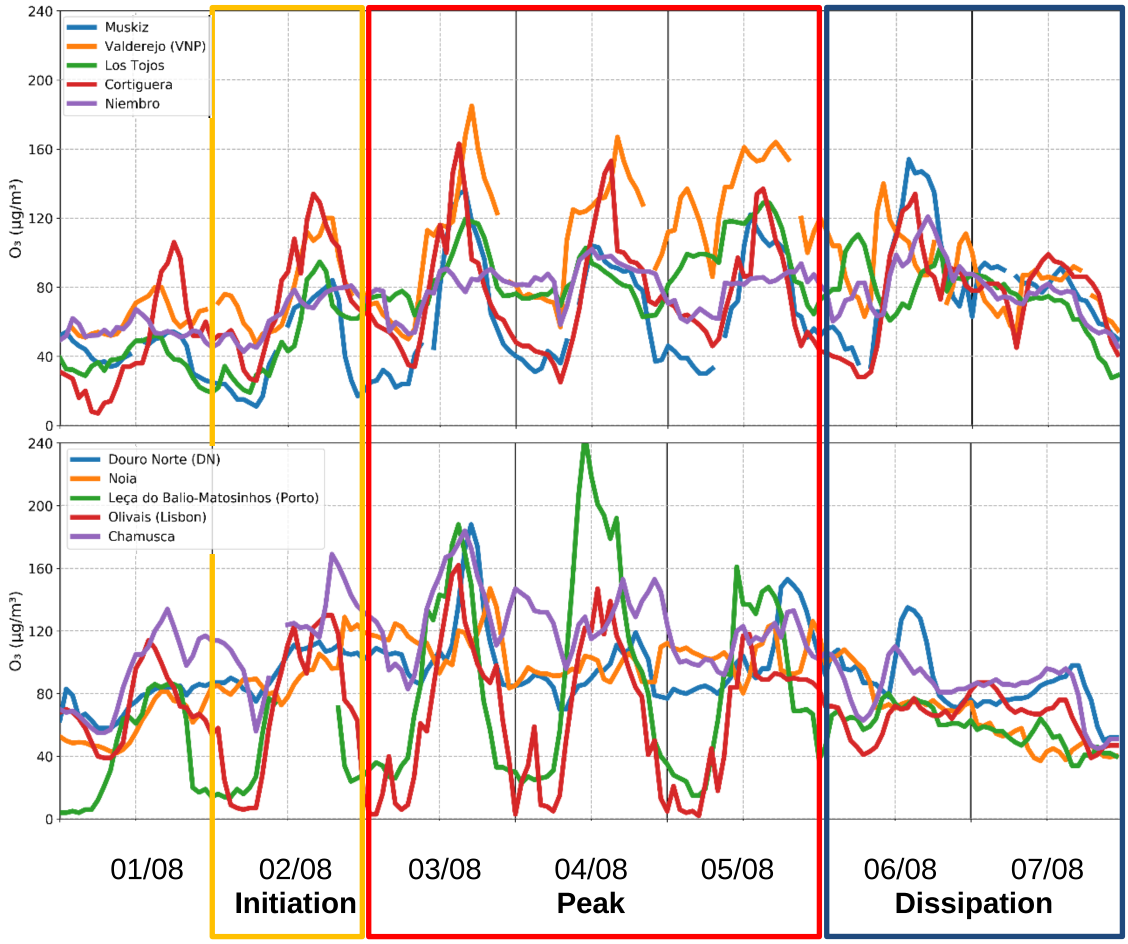

Figure 8. Ozone hourly concentrations time sequences for 1-7 August 2018 at a selection of stations along Northern Atlantic Iberia (top) and Western Atlantic Iberia (bottom).

3.3.1. Initiation

During August 1, an accumulation of O_3 integrated up to 2,500 m AGL of more than 135 ppm·m in the center of IP, northern coast of Portugal, Western Mediterranean Basin, and NE of IP has been simulated (Figure 9 a.2). The winds at altitude, from E and SE, suggest the beginning of the transport of O_3 and other pollutants from E to W of IP. At the surface, the highest concentrations were found in the simulation towards NW of Madrid and N of Barcelona due to the impact of emissions from these metropolitan areas, a pattern that is constantly repeated throughout the episode (Figure 9 a.1 and b.1). Concentrations in WAI began to rise, up to 95-105 μg·m^{-3}, while in NAI remained low with 75-85 μg·m^{-3}, probably due to a lower photochemical production under cloudier skies (see Figure S1).

On August 2, the air recirculation in the upper-layers (Figure 9 b.2), with completely clear skies and stagnant winds, caused an increase in surface O_3 concentrations to values exceeding 130 μg·m^{-3}, compared to the approximately 100 μg·m^{-3} from the previous day (Figure 9 b.1). That increase of more than 30 μg·m^{-3} over surface simulated concentrations, and more than 40 μg·m^{-3} over measured maximum concentrations both in NAI and WAI (Figure 8), together with the displacement of the high-altitude O_3-rich air masses towards NAI and WAI, support the hypothesis of fumigation of pollutants as the main cause of the observed surface ozone increases during that day. We have analyzed vertical atmosphere cross-sections in VNP and DN to address this hypothesis.

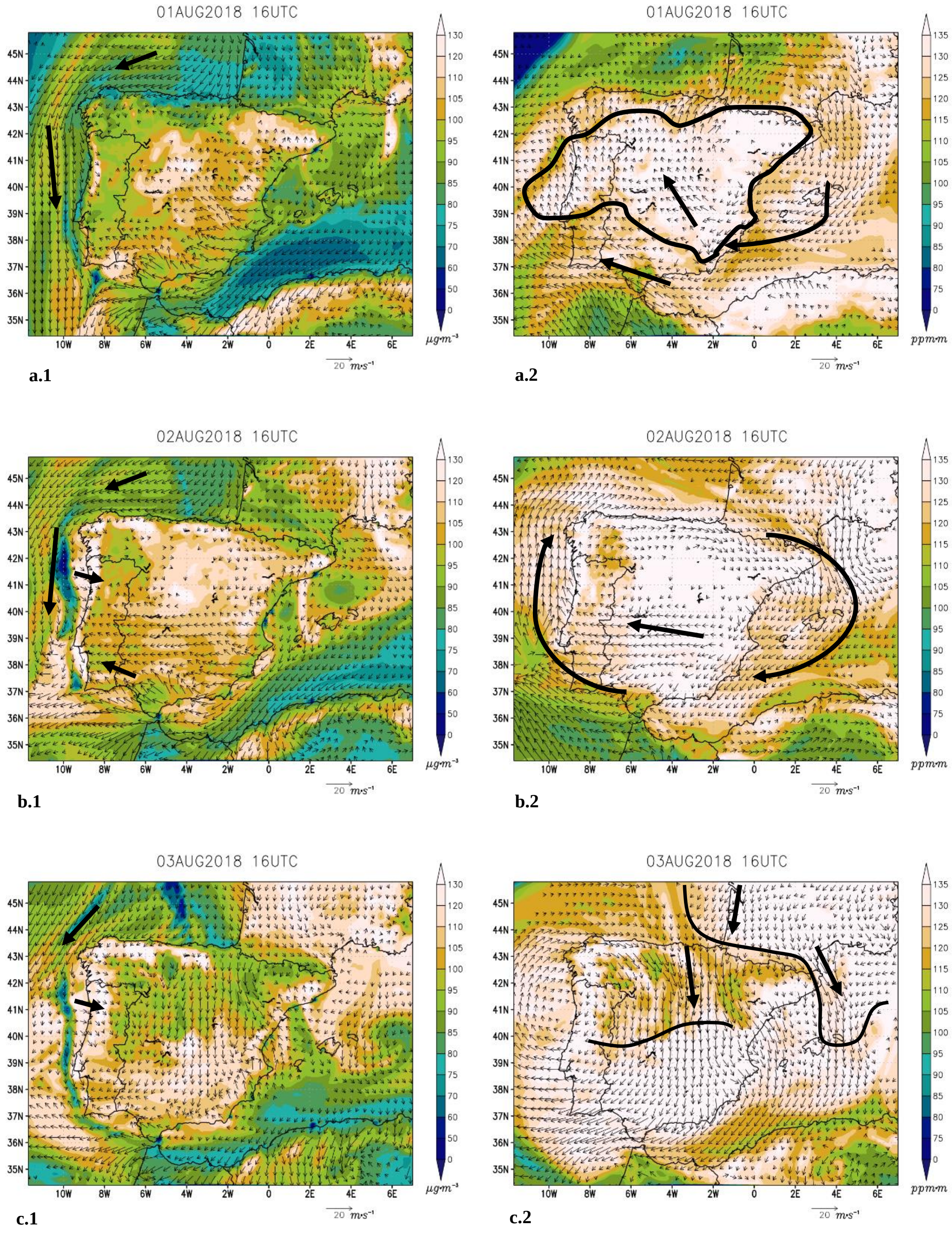

Figure 9. Simulated O_3 concentrations (color scale) and wind fields (vectors) by WRF-CAMx in d02 at 16 UTC on August 1, 2 and 3, 2018. Left panels show the ozone and wind concentration in surface and right panels the integrated ozone concentration up to 2500 m AGL and wind at 1250 m AGL. Winds lower than 2 m·s^{-1} have been omitted.

In VNP, on August 1, the higher polluted air mass was positioned above 1,800 meters above sea level (ASL) as indicated by the simulated O_3 concentrations (Figure 10 a. and b). On August 2, starting from 12 UTC, this high-altitude polluted air mass was mixed with surface air masses in the inland valleys. This led to simulated O_3 concentrations exceeding 110 µg·m^{-3} (55 ppb as shown in Figure 10 c). Winds at a horizontal projection above 500 m ASL were from S, while below 500 m ASL sea breezes from N prevailed near the coast, resulting in O_3 concentrations not significantly high along the coastal areas (40 ppb). By the afternoon of August 2 (Figure 10 d), winds at a horizontal projection above 1,000 m ASL shifted to the N, causing the polluted air mass to recede towards the south of the IP. Consequently, the initial peak observed in Valderejo on day 2 (as depicted in Figure 8) was a result of this fumigation process. From August 3 onwards (Figure 10 e and f), we observed the influx of O_3 polluted air masses of European origin below 1,500 m ASL transported across the sea.

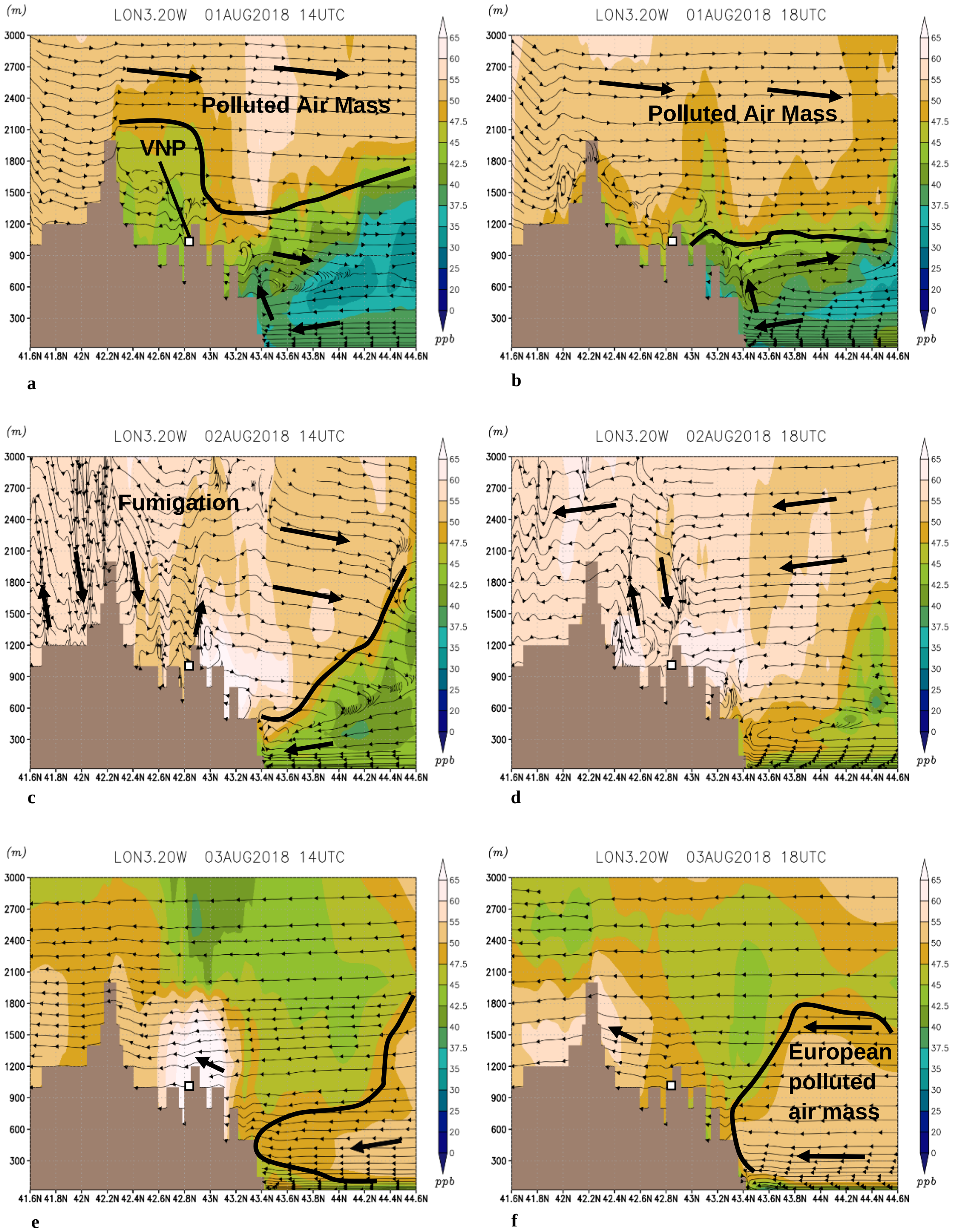

Figure 10. Simulated vertical O_3 concentrations (color scale) and projected wind fields (stream composed by projected u with w(*10)) by WRF-CAMx in d03 at 14 UTC and 18 UTC on August 1, 2 and 3, 2018, for the VNP vertical cross-section. Concentrations are depicted in ppb as they are altitude independent (1 ppb ≈ 2 $\mu g \cdot m^{-3}$ at sea level).

In DN, on August 1, an upper-level polluted air mass entered at approximately 1,800 meters above sea level (ASL) originated in the S/SW (Figure 11 a). While low O_3 concentrations were observed over the sea surface, a slight increase in concentrations occurred along the coastline in the lower atmospheric layers between 400 and 1,000 meters ASL. Inland valleys experienced high O_3 concentrations due to the pollution carried at higher altitudes and mixed into the surface, propelled by convective movements during the afternoon (Figure 11 b). Return flows along the coast at 900 meters ASL during the afternoon (Figure 11 b) potentially carried some of this elevated O_3 back to the sea surface, creating an O_3 reservoir for subsequent days. This mechanism resembles processes described for Mediterranean regions (Millán et al., 2002), resulting in sea-land recirculations over several consecutive days, forming injections of ozone into upper layers that may return to the coast during the following days (Figure 11 from c to f).

In addition to the fumigation process, surface winds during midday on August 1 and 2 were northerly over WAI and northeasterly over the Bay of Biscay. That could infer a transport of pollutants from the French Atlantic coast towards WAI in the lower layers of the atmosphere (Figure 9 a.1, b.1 and c.1) as documented in Gangoiti et al. (2006a), although that transport was more evident from August 3 onwards.

Those two possible O_3 transport pathways (fumigation and regional transport) would be responsible for the significant increase in O_3 concentrations in WAI, up to 160 $\mu g\text{-}m^{-3}$ measured inland during the afternoon on August 2 (see Chamusca station in Figure 8) with the onset of the sea breezes (Figure 9 a.1, b.1 and c.1). The plume generated on the coast was transported inland and injected through orographic chimneys to the existing recirculating air mass in upper layers, reaching up to 2,400 m ASL.

3.3.2. Peak

During August 3, the change in synoptic conditions led to the transport of the polluted air mass from N to S of the peninsula (Figure 9 c.2). At the same time, the SE winds from the previous day over the SW of IP dragged part of the polluted air mass toward the coast of Portugal, causing an accumulation of O_3 over WAI (Figure 9 c.2). On the surface, as on August 2, WRF-CAMx-simulated O_3 concentrations were above 130 $\mu g \cdot m^{-3}$ over NAI and WAI (Figure 9 b.1). The wind shift to N-NE at the end of August 3 caused the entry of new polluted air masses from France, both through the Bay of Biscay towards NAI and through the Gulf of Lion towards the Mediterranean Sea. That transport pathway corroborates one of the accumulation phase transport pathways proposed by Gangoiti et al. (2006a) and Valdenebro et al. (2011). In this episode, however, there was no previous gradual accumulation, it already started with an abrupt rise in O_3 concentrations on the previous two days, during the initiation.

Particularly in WAI, during August 2 and 3 there is a notable increase in the O_3 simulated concentrations over the sea (Figure 11 c, d, e and f). We have observed that during August 3 PM_{10} measured concentrations in Western IP increased notably, up to 60 $\mu g \cdot m^{-3}$. These high concentrations lasted until August 5 (not shown in this paper), and they were concurrent with lower O_3 concentrations in upper layers (Figure 11 c, d, e and f), indicating a transport of mineral dust from the Sahara Desert to the WAI. Fumigation processes on August 2 would have transported O_3 from the upper layers to the surface, whereas on August 3 it would be dust instead of O_3 (see the dust location in the satellite map in Figure S1). Those fumigation processes could introduce O_3 and PM into the sea-land recirculation cells causing high measured concentrations of both pollutants simultaneously.

In the VNP, over NAI, an intrusion of polluted air through the Bay of Biscay from the North, of French origin, was observed, causing O_3 concentrations of 100 $\mu g \cdot m^{-3}$ (50 ppb) from surface level to 1,500 m ASL (Figure 10 e and f). Additionally, we observed how local pollutants emitted on the coastline impacted the inland valleys, producing more than 160 $\mu g \cdot m^{-3}$ of O_3 (Figure S9). Thus, a significant local contribution was added to the already existing regional transport of polluted air masses. In DN, over WAI, the pattern of inflow with the sea breeze and impact on inland areas was repeated as shown in Figure S10, also documented in other studies (Evtyugina et al., 2007; Monteiro et al., 2012, 2016; Torre-Pascual et al., 2023).

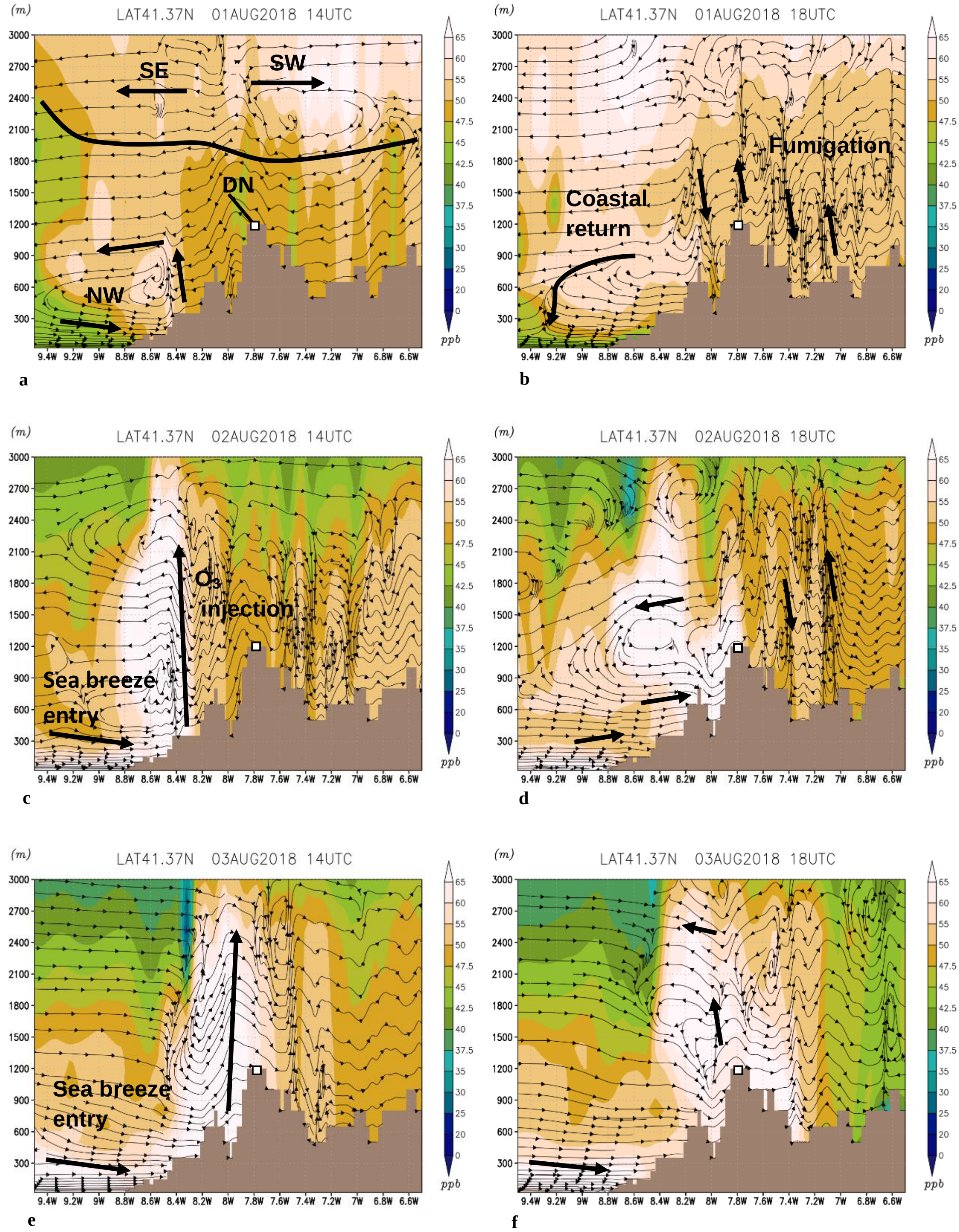

Figure 11. Simulated vertical O_3 concentrations (color scale) and projected wind fields (stream composed by projected v with w(*10)) by WRF-CAMx in d03 at 14 UTC and 18 UTC on August 1, 2 and 3, 2018 for the DN vertical cross-section. Concentrations are depicted in ppb as they are altitude independent (1 ppb ≈ 2 $\mu g \cdot m^{-3}$ at sea level).

During August 4 and 5 the simulated surface O_3 concentrations exceeded again 130 $\mu g \cdot m^{-3}$ on NAI and WAI (not shown). The transport of pollutants from France to NAI through the Gulf of Biscay and to the Mediterranean Sea through the Gulf of Lion continued during those days and cycles of sea-breezes were repeated. In the case of the Douro Norte station, we observed the transport of polluted air masses from the coast into that area due to the sea-breeze. A sudden rise in O_3 hourly concentrations occurring on August

3, 5, and 6 was caused by the impacts of these air masses, but not with such intensity on August 4 (Figure S10) because of a more Southerly trajectory during that day of the polluted air mass (not shown). The approach of the cold front during August 5 caused prefrontal winds of W-SW component over IP that initiated the transport of all pollutants from the W to the E of IP.

3.3.3. Dissipation

The Atlantic air mass entered IP on August 6, introducing cloudiness (Figure S1) and producing wind shift to W over WAI. That change introduced cleaner air to the west of the peninsula (Figure 12). However, in NAI, O_3-polluted air masses coming from the W and SW of Iberia were transported with the prefrontal winds, adding O_3 to the one previously accumulated days before (Figure 12 a.1 and a.2). That situation caused high simulated O_3 surface concentrations (> 130 µg·m^{-3}) and the highest observations over NAI (Figure 7 and Figure 8). The passage of the frontal system generated a simulated "ozone front" also confirmed by the measurements. The final entry of cleaner air from the Atlantic Ocean during August 7 significantly reduced O_3 concentrations both at the surface and in altitude in the NW region of IP (Figure 12 b.1 and b.2). In the E of IP and the Western Mediterranean Basin, higher concentrations were still found in the simulations, indicating a possible episode during the following days in that territory.

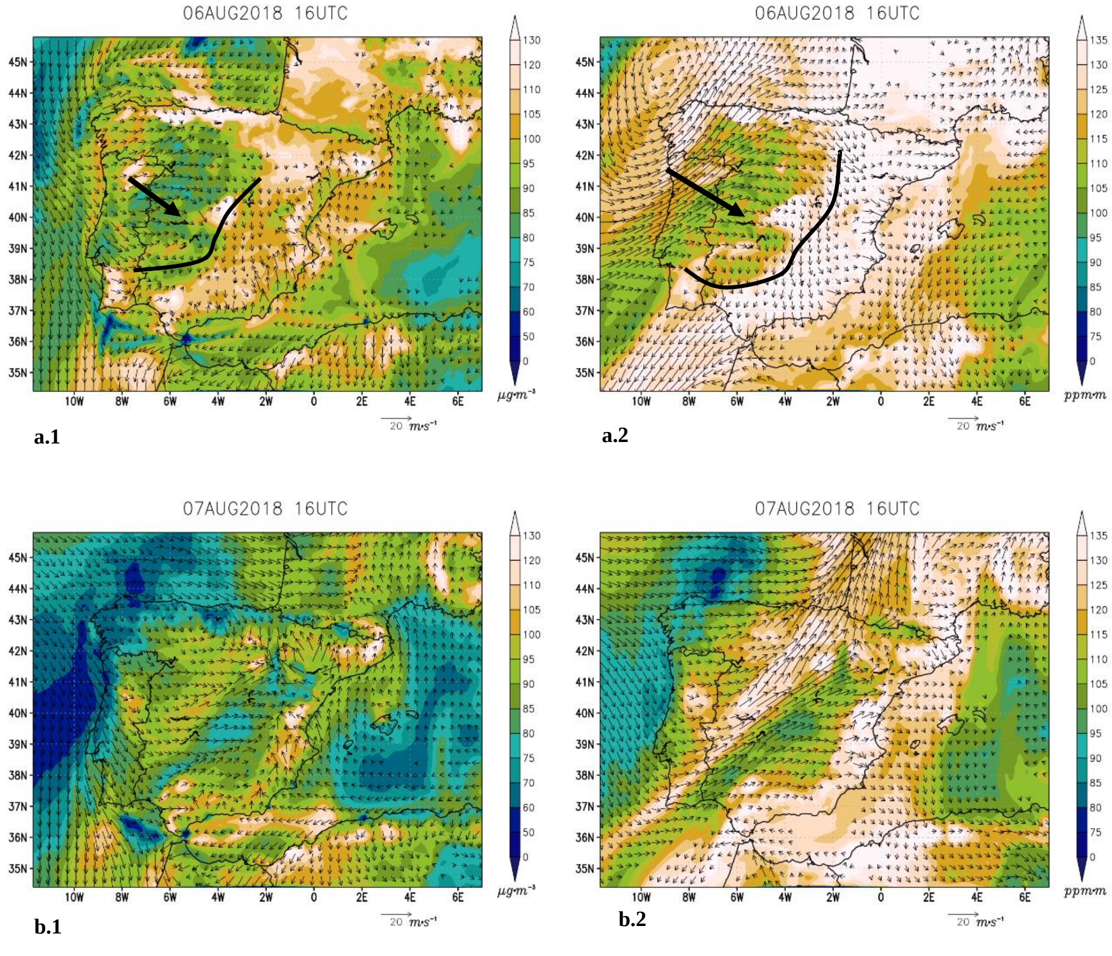

Figure 12. Simulated O_3 concentrations (color scale) and wind fields (vectors) by WRF-CAMx in d02 at 16 UTC on August 6 and 7, 2018. Left panels show the ozone and wind concentration in surface and right panels the integrated ozone concentration up to 2500 m AGL and wind at 1250 m AGL. Winds lower than 2 m·s^{-1} have been omitted.

4. Conclusions

This paper analyzes a tropospheric O_3 pollution episode that occurred over WAI and NAI, in Spain and Portugal, during August 2-6, 2018. The episode was characterized by an almost-simultaneous abrupt rise in O_3 concentrations in both regions, which remained high throughout the entire episode, exceeding the target values and the information threshold of the EC/50/2008 EU Directive. Using the meteorological and photochemical WRF-CAMx modeling system, we have identified the transport mechanisms behind this type of episodes, especially complex due to a meteorology characterized by a permanent wind shear throughout the entire period. Additionally, we have been able to characterize the possible sources of photochemical pollutants affecting these two areas.

The episode began with an accumulation of pollutants in the higher layers above 2,000 m AGL over IP, due to a decoupling of high altitude and surface air masses. The origin of that upper-level polluted air mass was probably due to the emission of pollutants during previous days in IP itself, which were then trapped in below 2,500 m ASL due to the stability of the upper warmer air. Subsequently, upper air masses fumigated onto the surface through the different orographic chimneys along the Atlantic coast, producing the beginning of the episode. During the initiation of the episode, the simulation pointed out that the dominant process was likely to be fumigation, with a contribution of 30-40 $\mu g \cdot m^{-3}$ of the observed O_3 increase. Measured O_3 maximum daily concentrations increased in more than 40 $\mu g \cdot m^{-3}$ from the previous day's highs, and simulated O_3 in more than 30 $\mu g \cdot m^{-3}$.

From August 3 onwards, the fumigated air masses were joined by other polluted air masses. According to the simulation, NAI received O_3-polluted air masses imported from France, providing a minimum of 100 $\mu g \cdot m^{-3}$ background O_3 concentrations, while WAI received O_3 from the N and center of IP, probably sharing the same minimum background contribution because of the continuity of those air masses. The most intense exceedances occurred in the sea-facing slopes of the main coastal ranges, at Valderejo (Basque Country, Spain) and Douro Norte (Portugal) measurement stations. In these sites, there is an additional impact of local coastal emissions to the already existing high background concentrations (100 $\mu g \cdot m^{-3}$). That local contribution, introducing "fresh" pollutants inland with the sea breezes, produced concentrations above 130 $\mu g \cdot m^{-3}$ of O_3 in the form of a peak of both measured and simulated concentrations, indicating a local contribution of at least 30 $\mu g \cdot m^{-3}$ of O_3 in both locations. Those concentrations, as well as the transport pathways observed through the simulations, showed that during the episode there were different contributions and interrelated transport processes, first, an O_3 fumigation and interregional transport (within IP) during August 2, and then, from August 3 onwards, a continental European O_3 transport and concurrent accumulation within coastal circulations. The dissipation of the episode occurred gradually from W to E due to an Atlantic advection, which introduced colder and cleaner air. After the front passed through, pollutants were carried from W to E, causing maximum hourly concentrations that were significant prior to the episode dissipation.

CAMx simulation conformed to the statistical parameters traditionally used with these models. We have introduced for the first time the analysis of winds in altitude and the calculation of integrated O_3 concentrations for a deeper understanding of this episode. These newly proposed analyses are necessary to understand air pollution episodes in areas with complex topography where re-circulatory processes can occur in both the upper and lower atmosphere. They allowed us to observe the medium and long-range transports of polluted air masses, abstracting from local effects, and, in turn, whether the increases in O_3 concentrations were due to air mass horizontal advections, fumigations, or a combination of both.

In view of the diversity of processes involved in this type of O_3 episodes, the authors of this article recommend extending the analysis of modeling studies to upper levels of the atmosphere, particularly in complex terrain applications and with complex meteorological situations such as this case. In order to improve predictions as well as control strategies, databases of observations should be expanded at the surface and upper levels of the atmosphere. WAI surface station measurements have proven to be representative for evaluating the episode and agree with the simulations. Meanwhile, in NAI, measurement stations might not be very representative to address this kind of episodes due to their proximity to industrial sites. In upper levels of the atmosphere, O_3 soundings and LIDAR, among other techniques for the characterization of the vertical ozone distribution, should be used to further analyze the transport pathways and accumulation processes addressed in this paper.

Author contributions

Eduardo Torre-Pascual: Conceptualization, Data curation, Formal analysis, Investigation, Software, Visualization, Original draft preparation, Review & Editing.
Gotzon Gangoiti: Conceptualization, Data curation, Formal analysis, Investigation, Software, Visualization, Original draft preparation, Review & Editing.
Ana Rodríguez-García: Conceptualization, Data curation, Formal analysis, Investigation, Software, Visualization, Original draft preparation, Review & Editing.
Estibaliz Sáez de Cámara: Conceptualization, Data curation, Investigation, Software, Visualization, Original draft preparation, Review & Editing.
Joana Ferreira: Conceptualization, Data curation, Investigation, Visualization, Original draft preparation, Review & Editing.
Carla Gama: Conceptualization, Data curation, Investigation, Visualization, Original draft preparation, Review & Editing.
María Carmen Gómez: Conceptualization, Investigation, Visualization, Original draft preparation, Review & Editing.
Iñaki Zuazo: Conceptualization, Data curation, Investigation, Visualization, Original draft preparation, Review & Editing.
Jose Antonio García: Conceptualization, Investigation, Visualization, Original draft preparation, Review & Editing.
Maite de Blas: Conceptualization, Investigation, Visualization, Original draft preparation, Review & Editing.

Competing interests

The authors declare that they have no conflict of interest.

Acknowledgments

The authors wish to thank the Department of Economic Development, Sustainability and the Environment of the Basque Government (CONV 22/16) and the University of the Basque Country UPV/EHU as the source of our main financial support: GIA consolidated Research Groups (GIU21/050) (https://www.ehu.eus/es/web/gia). In addition to the Spanish Ministry of Universities and the European Union, for the Margarita Salas Grant (MARSA21/23) of Eduardo Torre-Pascual, funded by the European Union-Next Generation EU. These financing bodies have played an exclusively economic role in the study.

Thanks are also due for the financial support to the contract grants of J. Ferreira (2020.00622.CEECIND) and C. Gama (2021.00732.CEECIND), to CESAM (UIDP/50017/2020+ UIDB/50017/2020+ LA/P/0094/2020), to FCT/MCTES through national funds and the co-funding by the FEDER, within the PT2020 Partnership Agreement and Compete 2020.

References

Adame, J.A., Hernández-Ceballos, M.A., Bolívar, J.P., and De la Morena, B.: Assessment of an air pollution event in the southwestern Iberian Peninsula, Atmospheric Environment, 55, 245-256, https://doi-org.ehu.idm.oclc.org/10.1016/j.atmosenv.2012.03.010, 2012.

Alonso, L., Gangoiti, G., Navazo, M., Millán, M. M., and Mantilla, E.: Transport of Tropospheric Ozone over the Bay of Biscay and the Eastern Cantabrian Coast of Spain, Journal of Applied Meteorology, 39(4), 475-486, https://doi.org/10.1175/1520-0450(2000)039<0475:TOTOOT>2.0.CO;2, 2000.

Baldasano, J., Pay, M., Jorba, O., Gassó, S., and Jimenez-Guerrero, P.: An annual assessment of air quality with the CALIOPE modeling system over Spain, The Science of the total environment, 409, 2163-2178, https://doi.org/10.1016/j.scitotenv.2011.01.041, 2011.

Banks, R. F., and Baldasano, J. M.: Impact of WRF model PBL schemes on air quality simulations over Catalonia, Spain, Science of The Total Environment, 572, 98-113, https://doi.org/10.1016/j.scitotenv.2016.07.167, 2016.

Banzon, V., Smith, T. M., Chin, T. M., Liu, C., and Hankins, W.: A long-term record of blended satellite and in situ sea-surface temperature for climate monitoring, modeling and environmental studies, Earth System Science Data, 8(1), 165-176, https://doi.org/10.5194/essd-8-165-2016, 2016.

Berrisford, P., Dee, D. P., Poli, P., Brugge, R., Fielding, M., Fuentes, M., Kållberg, P. W., Kobayashi, S., Uppala, S., and Simmons, A.: The ERA-Interim archive Version 2.0. Report, ERA Report Series, ECMWF, Shinfield Park, Reading, 2011.

Bessagnet, B., Pirovano, G., Mircea, M., Cuvelier, C., Aulinger, A., Calori, G., Ciarelli, G., Manders, A., Stern, R., Tsyro, S., García Vivanco, M., Thunis, P., Pay, M. T., Colette, A., Couvidat, F., Meleux, F., Rouïl, L., Ung, A., Aksoyoglu, S., … White, L.: Presentation of the EURODELTA III intercomparison exercise – evaluation of the chemistry transport models' performance on criteria pollutants and joint analysis with meteorology, Atmospheric Chemistry and Physics, 16(19), 12667-12701, https://doi.org/10.5194/acp-16-12667-2016, 2016.

Borge, R., Alexandrov, V., José del Vas, J., Lumbreras, J., and Rodríguez, E.: A comprehensive sensitivity analysis of the WRF model for air quality applications over the Iberian Peninsula, Atmospheric Environment, 42(37), 8560-8574, https://doi.org/10.1016/j.atmosenv.2008.08.032, 2008.

Borge, R., Lumbreras, J., Pérez, J., de la Paz, D., Vedrenne, M., de Andrés, J. M., and Rodríguez, M. E.: Emission inventories and modeling requirements for the development of air quality plans. Application to Madrid (Spain), Science of The Total Environment, 466-467, 809-819, https://doi.org/10.1016/j.scitotenv.2013.07.093, 2014.

Borrego, C., Monteiro, A., Ferreira, J., Miranda, A. I., Costa, A. M., Carvalho, A. C., and Lopes, M.: Procedures for estimation of modelling uncertainty in air quality assessment, Environment International, 34(5), 613-620, https://doi.org/10.1016/j.envint.2007.12.005, 2008.

Borrego, C., Souto, J. A., Monteiro, A., Dios, M., Rodríguez, A., Ferreira, J., Saavedra, S., Casares, J. J., and Miranda, A. I.: The role of transboundary air pollution over Galicia and North Portugal area, Environmental Science and Pollution Research, 20(5), 2924-2936, https://doi.org/10.1007/s11356-012-1201-9, 2013.

Borrego, C., Monteiro, A., Martins, H., Ferreira, J., Fernandes, A. P., Rafael, S., Miranda, A. I., Guevara, M., and Baldasano, J. M.: Air quality plan for ozone: An urgent need for North Portugal. Air Quality, Atmosphere & Health, 9(5), 447-460, https://doi.org/10.1007/s11869-015-0352-5, 2016.

Carvalho, A., Monteiro, A., Ribeiro, I., Tchepel, O., Miranda, A.I., Borrego, C., Saavedra, S., Souto, J.A., and Casares, J.J.: High ozone levels in the northeast of Portugal: Analysis and characterization, Atmospheric Environment, 44(8), 1020-1031, https://doi.org/10.1016/j.atmosenv.2009.12.020, 2010.

Copernicus Climate Change Service: ERA5: Fifth generation of ECMWF atmospheric reanalyses of the global climate, Copernicus Climate Change Service (C3S) Climate Data Store (CDS), https://cds.climate.copernicus.eu/cdsapp#!/datase t/reanalysis-era5-pressure-levels?tab=overview, 2018.

Cuevas, E., González, Y., Rodríguez, S., Guerra, J. C., Gómez-Peláez, A. J., Alonso-Pérez, S., Bustos, J., and Milford, C.: Assessment of atmospheric processes driving ozone variations in the subtropical North Atlantic free troposphere, Atmos. Chem. Phys., 13, 1973–1998, https://doi.org/10.5194/acp-13-1973-2013, 2013.

Crippa, M., Guizzardi, D., Muntean, M., Schaaf, E., Dentener, F., van Aardenne, J. A., Monni, S., Doering, U., Olivier, J. G. J., Pagliari, V., and Janssens-Maenhout, G.: Gridded emissions of air pollutants for the period 1970–2012 within EDGAR v4.3.2, Earth System Science Data, 10(4), 1987-2013, https://doi.org/10.5194/essd-10-1987-2018, 2018.

de Blas, M., Ibáñez, P., García, J. A., Gómez, M. C., Navazo, M., Alonso, L., Durana, N., Iza, J., Gangoiti, G., and Sáez de Cámara, E.: Summertime high resolution variability of atmospheric formaldehyde and non-methane volatile organic compounds in a rural background area, Science of The Total Environment, 647, 862-877, https://doi.org/10.1016/j.scitotenv.2018.07.411, 2019.

Denier van der Gon, H.A.C., Hendriks, C., Kuenen, J., Segers, A., Visschedijk, A.J.H.: Description of current temporal emission patterns and sensitivity of predicted AQ for temporal emission patterns. EU FP7 MACC deliverable report D_D-EMIS_1.3, https://atmosphere.copernicus.eu/sites/default/files/2019-07/MACC_TNO_del_1_3_v2.pdf, 2011.

EEA: European Environment Agency. Technical report No 11. Guidance report on preliminary assessment under EC air quality directives. Chapter 4. Human activity and emission inventories, https://www.eea.europa.eu/publications/TEC11a/page010.html, 2016.

EEA: European Environment Agency. Air quality in Europe - 2018 report, Guerreiro, C., Colette, A., Leeuw, F., and González Ortiz, A., Publications Office, http://doi.org/10.2800/777411, 2019.

EEA: European Environment Agency. Europe's air quality status 2022, Briefing no. 04/2022, http://doi.org/10.2800/049755, 2022.

EPA: U.S. Environmental Protection Agency. SPECIATE Version 4.5. Database Development Documentation. EPA/600/R-16/294, https://www.epa.gov/sites/default/files/2016-09/documents/speciate_4.5.pdf, 2016.

Escudero, M., Segers, A., Kranenburg, R., Querol, X., Alastuey, A., Borge, R., de la Paz, D., Gangoiti, G., and Schaap, M.: Analysis of summer O3 in the Madrid air basin with the LOTOS-EUROS chemical transport model, Atmospheric Chemistry and Physics, 19(22), 14211-14232, https://doi.org/10.5194/acp-19-14211-2019, 2019.

ETC/ACM: European Topic Centre on Air Pollution and Climate Change Mitigation, Ozone in southern Europe – Assessment and effectiveness of measures, Technical Paper 2017/3, https://www.eionet.europa.eu/etcs/etc-atni/products/etc-atni-reports/etcacm_tp_2017_3_ozone_s-europe, 2018.

Evtyugina, M.G., Pio, C., Nunes, T., Pinho, P.G., and Costa, C.S.: Photochemical ozone formation at Portugal West Coast under sea breeze conditions as assessed by master chemical mechanism model, Atmospheric Environment, 41(10), 2171-2182, https://doi-org.ehu.idm.oclc.org/10.1016/j.atmosenv.2006.10.059, 2007.

Evtyugina, M. G., Nunes, T., Alves, C., and Marques, M. C.: Photochemical pollution in a rural mountainous area in the northeast of Portugal, Atmospheric Research, 92(2), 151-158, https://doi.org/10.1016/j.atmosres.2008.09.006, 2009.

Gangoiti, G., Millán, M.M., Salvador, R., and Mantilla, E.: Long-range transport and re-circulation of pollutants in the western Mediterranean during the project Regional Cycles of Air Pollution in the West-Central Mediterranean Area, Atmospheric Environment, 35(36), 6267-6276, https://doi.org/10.1016/S1352-2310(01)00440-X, 2001.

Gangoiti, G., Alonso, L., Navazo, M., Albizuri, A., Pérez-Landa, G., Matabuena, M., Valdenebro, V., Maruri, M., García, J.A., and Millán, M.M.: Regional transport of pollutants over the Bay of Biscay: analysis of an ozone episode under a blocking anticyclone in west-central Europe, Atmospheric Environment, 36, 1349-1361, https://doi.org/10.1016/S1352-2310(01)00536-2, 2002.

Gangoiti, G., Albizuri, A., Alonso, L., Navazo, M., Matabuena, M., Valdenebro, V., García, J.A., and Millán, M.M.: Sub-continental transport mechanisms and pathways during two ozone episodes in northern Spain, Atmospheric Chemistry and Physics, 6(6), 1469-1484, https://doi.org/10.5194/acp-6-1469-2006, 2006a.

Gangoiti, G., Alonso, L., Navazo, M., García, J.A., and Millán, M.M.: North African soil dust and European pollution transport to America during the warm season: Hidden links shown by a passive tracer simulation, Journal of Geophysical Research: Atmospheres, 111(D10), https://doi.org/10.1029/2005JD005941, 2006b.

Gangoiti, G., de Blas, M., Gómez, M. C., Rodríguez-García, A., Torre-Pascual, E., García-Ruiz, E., Sáez de Cámara, E., Zuazo, I., García, J.A., and Valdenebro, V.: Impact of the COVID-19 Lockdown in a European Regional Monitoring Network (Spain): Are We Free from Pollution Episodes?, International Journal of Environmental Research and Public Health, 18(21), https://doi.org/10.3390/ijerph182111042, 2021.

Gómez, M.C., Durana, N., García, J.A., de Blas, M., Sáez de Cámara, E., García-Ruiz, E., Gangoiti, G., Torre-Pascual, E., and Iza, J.: Long-term measurement of biogenic volatile organic compounds in a rural background area: Contribution to ozone formation, Atmospheric Environment, 224, 117315, https://doi.org/10.1016/j.atmosenv.2020.117315, 2020.

Guenther, A., Karl, T., Harley, P., Wiedinmyer, C., Palmer, P. I., and Geron, C.: Estimates of global terrestrial isoprene emissions using MEGAN (Model of Emissions of Gases and Aerosols from Nature), Atmospheric Chemistry & Physics Discussions, 6, 107-173, https://doi.org/10.5194/acp-6-3181-2006, 2006.

Guenther, A. B., Jiang, X., Heald, C. L., Sakulyanontvittaya, T., Duhl, T., Emmons, L. K., and Wang, X.: The Model of Emissions of Gases and Aerosols from Nature version 2.1 (MEGAN2.1): An extended and updated framework for modeling biogenic emissions, Geoscientific Model Development, 5(6), 1471-1492, https://doi.org/10.5194/gmd-5-1471-2012, 2012.

Guenther, A.: BVOC Emission modeling. MEGAN BVOC Emissions training course. National University of Colombia, August 15-17, https://drive.google.com/file/d/0B53BwxgQlv_3TTJWbU1MQlFZOGs/view, 2017.

Hersbach, H., Bell, B., Berrisford, P., Hirahara, S., Horányi, A., Muñoz-Sabater, J., Nicolas, J., Peubey, C., Radu, R., Schepers, D., Simmons, A., Soci, C., Abdalla, S., Abellan, X., Balsamo, G., Bechtold, P., Biavati, G., Bidlot, J., Bonavita, M., De Chiara, G., Dahlgren, P., Dee, D., Diamantakis, M., Dragani, R., Flemming, J., Forbes, R., Fuentes, M., Geer, A., Haimberger, L., Healy, S., Hogan, R.J., H´ olm, E., Janiskov´a, M., Keeley, S., Laloyaux, P., Lopez, P., Lupu, C., Radnoti, G., de Rosnay, P., Rozum, I., Vamborg, F., Villaume, S.: The´paut, J.-N.: The ERA5 global reanalysis. Q. J. R. Meteorol. Soc., 146, 1999–2049, https://doi.org/10.1002/qj.3803, 2020.

Hertig, E., Russo, A., and Trigo, R. M.: Heat and Ozone Pollution Waves in Central and South Europe — Characteristics, Weather Types, and Association with Mortality, Atmosphere, 11(12), Art. 12, https://doi.org/10.3390/atmos11121271, 2020.

Hong, S.-Y., Noh, Y., and Dudhia, J.: A New Vertical Diffusion Package with an Explicit Treatment of Entrainment Processes, Monthly Weather Review, 134, 2318-2341, http://dx.doi.org/10.1175/MWR3199.1, 2006.

in ’t Veld, M., Carnerero, C., Massagué, J., Alastuey, A., de la Rosa, J. D., Sánchez de la Campa, A. M., Escudero, M., Mantilla, E., Gangoiti, G., García-Pando, C. P., Olid, M., Moreta, J. R., Hernández, J. L., Santamaría, J., Millán, M., and Querol, X.: Understanding the local and remote source contributions to ambient O3 during a pollution episode using a combination of experimental approaches in the Guadalquivir valley, southern Spain. Science of The Total Environment, 777, 144579, https://doi.org/10.1016/j.scitotenv.2020.144579, 2021.

Janssens-Maenhout, G., Crippa, M., Guizzardi, D., Muntean, M., Schaaf, E., Dentener, F., Bergamaschi, P., Pagliari, V., Olivier, J. G. J., Peters, J. A. H. W., van Aardenne, J. A., Monni, S., Doering, U., Petrescu, A. M. R., Solazzo, E., and Oreggioni, G. D.: EDGAR v4.3.2 Global Atlas of the three major greenhouse gas emissions for the period 1970–2012, Earth System Science Data, 11(3), 959-1002, https://doi.org/10.5194/essd-11-959-2019, 2019.

Jiménez, P., Lelieveld, J., and Baldasano, J. M.: Multiscale modeling of air pollutants dynamics in the northwestern Mediterranean basin during a typical summertime episode, Journal of Geophysical Research: Atmospheres, 111(D18), https://doi.org/10.1029/2005JD006516, 2006.

Knapp, K. R.: Scientific data stewardship of International Satellite Cloud Climatology Project B1 global geostationary observations, Journal of Applied Remote Sensing, 2, 023548, http://doi:10.1117/1.3043461, 2008.

Lamarque, J.-F., Emmons, L. K., Hess, P. G., Kinnison, D. E., Tilmes, S., Vitt, F., Heald, C. L., Holland, E. A., Lauritzen, P. H., Neu, J., Orlando, J. J., Rasch, P. J., and Tyndall, G. K.: CAM-chem: Description and evaluation of interactive atmospheric chemistry in the Community Earth System Model, Geoscientific Model Development, 5(2), 369-411, https://doi.org/10.5194/gmd-5-369-2012, 2012.

Massagué, J., Contreras, J., Campos, A., Alastuey, A., and Querol, X.: 2005–2018 trends in ozone peak concentrations and spatial contributions in the Guadalquivir Valley, southern Spain, Atmospheric Environment, 254, 118385, https://doi-org.ehu.idm.oclc.org/10.1016/j.atmosenv.2021.118385, 2021.

Millán, M.M., Artíñano, B., Alonso, L., Castro, M., Patier, R., and Goberna, J.: Meso-meteorological cycles of air pollution in the iberian peninsula, (MECAPIP), Contract EV4V-0097-E, Air Pollution Research Report 44, (Eur No. 14834) CEC-DG XII/E-1, Rue de la Loi, 200, 1992.

Millán, M.M., Salvador, R., Mantilla, E., and Kallos, G.: Photooxidant dynamics in the Mediterranean basin in summer: Results from European research projects, Journal of Geophysical Research: Atmospheres, 102(D7), 8811-8823, https://doi.org/10.1029/96JD03610, 1997.

Millán, M.M., Sanz, M.J., Salvador, R., and Mantilla, E.: Atmospheric dynamics and ozone cycles related to nitrogen deposition in the western Mediterranea, Environmental Pollution, 118(2), 167-18,. https://doi.org/10.1016/S0269-7491(01)00311-6, 2002.

Mlawer, E. J., Taubman, S. J., Brown, P. D., Iacono, M. J., and Clough, S. A.: Radiative transfer for inhomogeneous atmospheres: RRTM, a validated correlated-k model for the longwave, Journal of Geophysical Research: Atmospheres, 102(D14), 16663-16682, https://doi.org/10.1029/97JD00237, 1997.

Monteiro, A., Carvalho, A., Tchepel, O., Ferreira, J., Martins, H., Miranda, A., Borrego, C., Saavedra, S., Rodríguez, A., and Souto, J. A.: Photochemical Air Pollution in the North of Portugal: a High Tropospheric Ozone Episode, AGU Fall Meeting Abstracts, 21, A21C-0186, 2009.

Monteiro, A., Strunk, A., Carvalho, A., Tchepel, O., Miranda, A. I., Borrego, C., Saavedra, S., Rodríguez, A., Souto, J., Casares, J., Friese, E., and Elbern, H.: Investigating a high ozone episode in a rural mountain site, Environmental Pollution, 162, 176-189, https://doi.org/10.1016/j.envpol.2011.11.008, 2012.

Monteiro, A., Gama, C., Cândido, M., Ribeiro, I., Carvalho, D., Lopes, M.: Investigating ozone high levels and the role of sea breeze on its transport, Atmospheric Pollution Research, 7(2), 339-347, https://doi-org.ehu.idm.oclc.org/10.1016/j.apr.2015.10.013, 2016.

Myneni, R. B., Hoffman, S., Knyazikhin, Y., Privette, J. L., Glassy, J., Tian, Y., Wang, Y., Song, X., Zhang, Y., Smith, G. R., Lotsch, A., Friedl, M., Morisette, J. T., Votava, P., Nemani, R. R., and Running, S. W.: Global products of vegetation leaf area and fraction absorbed PAR from year one of MODIS data, Remote Sensing of Environment, 83(1), 214-231, https://doi.org/10.1016/S0034-4257(02)00074-3, 2002.

Navazo, M., Durana, N., Alonso, L., Gómez, M. C., García, J. A., Ilardia, J. L., Gangoiti, G., and Iza, J.: High temporal resolution measurements of ozone precursors in a rural background station. A two-year study, Environmental monitoring and assessment, 136, 53-68, https://doi.org/10.1007/s10661-007-9720-4, 2008.

NCAR: The National Center for Atmospheric Research, Tropospheric Ultraviolet and Visible (TUV) Radiation Model | Atmospheric Chemistry Observations & Modeling (ACOM), https://www2.acom.ucar.edu/modeling/tropospheric-ultraviolet-and-visible-tuv-radiation-model, 2011.

Nenes, A., Pandis, S. N., and Pilinis, C.: ISORROPIA: A New Thermodynamic Equilibrium Model for Multiphase Multicomponent Inorganic Aerosols, Aquatic Geochemistry, 4(1), 123-152, https://doi.org/10.1023/A:1009604003981, 1998.

Nenes, A., Pilinis, C., and Pandis, S. N.: Continued Development and Testing of a New Thermodynamic Aerosol Module for Urban and Regional Air Quality Models, Atmospheric Environment, 33, 1553-156, https://doi.org/10.1016/S1352-2310(98)00352-5, 1999.

Oikonomakis, E., Aksoyoglu, S., Ciarelli, G., Baltensperger, U., and Prévôt, A. S. H.: Low modeled ozone production suggests underestimation of precursor emissions (especially NOx) in Europe, Atmospheric Chemistry and Physics, 18(3), 2175-2198, https://doi.org/10.5194/acp-18-2175-2018, 2018.

Otte, T. L., and Pleim, J. E.: The Meteorology-Chemistry Interface Processor (MCIP) for the CMAQ modeling system: Updates through MCIPv3.4.1, Geoscientific Model Development, 3(1), 243-256, https://doi.org/10.5194/gmd-3-243-2010, 2010.

Pay, M. T., Piot, M., Jorba, O., Gassó, S., Gonçalves, M., Basart, S., Dabdub, D., Jiménez-Guerrero, P., and Baldasano, J. M.: A full year evaluation of the CALIOPE-EU air quality modeling system over Europe for 2004, Atmospheric Environment, 44(27), 3322-3342, https://doi.org/10.1016/j.atmosenv.2010.05.040, 2010.

Pay, M. T., Gangoiti, G., Guevara, M., Napelenok, S., Querol, X., Jorba, O., and Pérez García-Pando, C.: Ozone source apportionment during peak summer events over southwestern Europe, Atmospheric Chemistry and Physics, 19(8), 5467-5494, https://doi.org/10.5194/acp-19-5467-2019, 2019.

Pires, J.C.M., Alvim-Ferraz, M.C.M., Martins, F.G.: Surface ozone behaviour at rural sites in Portugal, Atmospheric Research, 104-105, 164-171, https://doi-org.ehu.idm.oclc.org/10.1016/j.atmosres.2011.10.001, 2012.

Querol, X., Alastuey, A., Reche, C., Orio, A., Pallares, M., Reina, F., Dieguez, J. J., Mantilla, E., Escudero, M., Alonso, L., Gangoiti, G., and Millán, M.: On the origin of the highest ozone episodes in Spain, Science of The Total Environment, 572, 379-389, https://doi.org/10.1016/j.scitotenv.2016.07.193, 2016.

Querol, X., Alastuey, A., Gangoiti, G., Perez, N., Lee, H. K., Eun, H. R., Park, Y., Mantilla, E., Escudero, M., Titos, G., Alonso, L., Temime-Roussel, B., Marchand, N., Moreta, J. R., Revuelta, M. A., Salvador, P., Artíñano, B., García dos Santos, S., Anguas, M., … Ahn, K.-H.: Phenomenology of summer ozone episodes over the Madrid Metropolitan Area, central Spain, Atmospheric Chemistry and Physics, 18(9), 6511-6533, https://doi.org/10.5194/acp-18-6511-2018, 2018.

Ramboll Environment and Health: User's Guide: Comprehensive Air Quality Model with Extensions. Version 6.5, Novato, California, https://camx-wp.azurewebsites.net/Files/CAMxUsersGuide_v6.50.pdf, 2018.

Rodrigues, V., Gama, C., Ascenso, A., Oliveira, K., Coelho, S., Monteiro, A., Hayes, E., and Lopes, M.: Assessing air pollution in European cities to support a citizen centered approach to air quality management, Sci. Total Environ., 799, 149311, https://doi.org/10.1016/j.scitotenv.2021.149311, 2021.

Russo, A., Gouveia, C., Levy, I., Dayan, U., Jerez, S., Mendes, M., and Trigo, R.: Coastal recirculation potential affecting air pollutants in Portugal: The role of circulation weather types, Atmos. Environ., 135, 9–19, https://doi.org/10.1016/j.atmosenv.2016.03.039, 2016.

Sá, E., Tchepel, O., Carvalho, A., and Borrego, C.: Meteorological driven changes on air quality over Portugal: A KZ filter application. Atmos. Pol. Res., 6(6), 979–989, https://doi.org/10.1016/j.apr.2015.05.003, 2015.

Sáez de Cámara, E., Gangoiti, G., Alonso, L., Valdenebro, V., Aksoyoglu, S., and Oikonomakis, E.: Ozone Source Apportionment to Quantify Local-to-Continental Source Contributions to Episodic Events in Northern Iberia, Air Pollution Modeling and its Application XXV, C. Mensink & G. Kallos (Eds.), 361-365, Springer Cham, https://doi.org/10.1007/978-3-319-57645-9_57, 2018.

Saha, S., Moorthi, S., Wu, X., Wang, J., Nadiga, S., Tripp, P., Behringer, D., Hou, Y.-T., Chuang, H., Iredell, M., Ek, M., Meng, J., Yang, R., Mendez, M. P., Dool, H. van den, Zhang, Q., Wang, W., Chen, M., and Becker, E.: The NCEP Climate Forecast System Version 2, Journal of Climate, 27(6), 2185-2208, https://doi.org/10.1175/JCLI-D-12-00823.1, 2014.

Silva, R.C.V. and Pires, J.C.M.: Surface Ozone Pollution: Trends, Meteorological Influences, and Chemical Precursors in Portugal, Sustainability, 14(4), 2383, https://doi.org/10.3390/su14042383, 2022.

Sindelarova, K., Granier, C., Bouarar, I., Guenther, A., Tilmes, S., Stavrakou, T., Müller, J.-F., Kuhn, U., Stefani, P., and Knorr, W.: Global data set of biogenic VOC emissions calculated by the MEGAN model over the last 30 years, Atmospheric Chemistry and Physics, 14(17), 9317-9341, https://doi.org/10.5194/acp-14-9317-2014, 2014.

Skamarock, W. C., Klemp, J. B., Dudhia, J., Gill, D. O., Barker, D., Duda, M. G., … Powers, J. G.: A Description of the Advanced Research WRF Version 3 (No. NCAR/TN-475+STR), University Corporation for Atmospheric Research, https://doi.org/10.5065/D68S4MVH, 2008.

Torre-Pascual, E., Sáez de Cámara, E., Gangoiti, G., and Zuazo, I.: Biogenic VOC Emission Modeling for Spain: Adaptation of the National Forest Inventory as Input for MEGANv3, Air Pollution Modeling and its Application XXVII, Mensink, C., Volker, M. (Eds.), 45-50, Springer, https://doi.org/10.1007/978-3-662-63760-9_7, 2021.

Torre-Pascual, E., Ferreira J., Sáez de Cámara E., Gama C., and Gangoiti G.: Ozone Episodes in Northern and Western Iberia: Understanding and Quantifying the Sources and Transport Mechanisms by Integrated Process Analysis, Air Pollution Modeling and its Application XXVIII, ITM 2021, Mensink, C., Jorba, O. (Eds.), Springer Proceedings in Complexity, Springer, Cham., https://doi.org/10.1007/978-3-031-12786-1_21, 2023.

Valdenebro, V., Gangoiti, G., Albizuri, A., Alonso, L., Navazo, M., García, J. A., Iza, J., and Millán, M. M.: Build-up and decay of two ozone episodes through northern Iberia and southern France - An inter-regional transport analysis, Atmospheric Environment, 45, 1595-1603, https://doi.org/10.1016/j.atmosenv.2010.12.031, 2011.

Valverde, V., Pay, M. T., and Baldasano, J. M.: Ozone attributed to Madrid and Barcelona on-road transport emissions: Characterization of plume dynamics over the Iberian Peninsula, Science of The Total Environment, 543, 670-682, https://doi.org/10.1016/j.scitotenv.2015.11.070, 2016.

Yang, W., Bin Tan, Dong Huang, Rautiainen, M., Shabanov, N. V., Wang, Y., Privette, J. L., Huemmrich, K. F., Fensholt, R., Sandholt, I., Weiss, M., Ahl, D. E., Gower, S. T., Nemani, R. R., Knyazikhin, Y., and Myneni, R. B.: MODIS leaf area index products: From validation to algorithm improvement, IEEE Transactions on Geoscience and Remote Sensing, 44(7), 1885-1898, https://doi.org/10.1109/TGRS.2006.871215, 2006.

Yuan, H., Dai, Y., Xiao, Z., Ji, D., and Shangguan, W.: Reprocessing the MODIS Leaf Area Index products for land surface and climate modelling, Remote Sensing of Environment, 115(5), 1171-1187, https://doi.org/10.1016/j.rse.2011.01.001, 2011.

Zhang, L., Gong, S., Padro, J., and Barrie, L.: A size-segregated particle dry deposition scheme for an atmospheric aerosol module, Atmospheric Environment, 35(3), 549-560, https://doi.org/10.1016/S1352-2310(00)00326-5, 2001.

Zhang, L., Brook, J. R., and Vet, R.: A revised parameterization for gaseous dry deposition in air-quality models, Atmospheric Chemistry & Physics, 3, 2067-2082, https://doi.org/10.5194/acp-3-2067-2003, 2003.

Zuazo, I., Torre-Pascual, E., and García, J. A.: Evaluation of Satellite Vegetation Indices for BVOC Emission Modelling. Case Study: Basque Country, Air Pollution Modeling and its Application XXVIII, ITM 2021, Mensink, C., Jorba, O. (Eds.), Springer Proceedings in Complexity, Springer, Cham., https://doi.org/10.1007/978-3-031-12786-1_41, 2023.